Domain organization and conformational change of dynactin p150

Kei Saito[1,*], Takashi Murayama[2,*], Tomone Hata[1], Takuya Kobayashi[2], Keitaro Shibata[1,†], Saiko Kazuno[3], Tsutomu Fujimura[3,#], Takashi Sakurai[2], and Yoko Y. Toyoshima[1]

[1]Department of Life Sciences, Graduate School of Arts and Sciences, The University of Tokyo, Meguro-ku, Tokyo 153-8902, Japan

[2] Department of Cellular and Molecular Pharmacology, Juntendo University Graduate School of Medicine, Bunkyo-ku, Tokyo 113-8421, Japan

[3]Laboratory of Proteomics and Biomolecular Science, BioMedical Research Center, Juntendo University Graduate School of Medicine, Bunkyo-ku, Tokyo 113-8421, Japan

*These authors contributed equally to this work.

Present addresses: [†]Advanced ICT Research Institute, National Institute of Information and Communications Technology, Kobe, Hyogo, Japan; [#]Laboratory of Bioanalytical Chemistry, Tohoku Medical and Pharmaceutical University, Miyagi, Japan

Corresponding author: Yoko Y. Toyoshima, E-mail; cyytoyo@mail.ecc.u-tokyo.ac.jp,

Tel; +81-3-5454-6752, Fax; +81-3-5454-6770

Abstract

Dynactin is a principal regulator of the minus-end directed microtubule motor dynein. The sidearm of dynactin is essential for binding to microtubules and regulation of dynein activity. Although our understanding of the structure of the dynactin backbone (Arp1 rod) has greatly improved recently, structural details of the sidearm part remain elusive. Here, electron microscopy of individual molecules of the dynactin complex revealed that the sidearm was highly flexible and exhibited diverse morphologies. Utilizing mutants for nanogold labeling and deletion analysis, we determined the domain organization of the largest subunit p150 and identified a filamentous structure protruding from the head domain of the sidearm as the coiled-coil 1 (CC1), the dynein-binding domain, in p150. Furthermore, the CC1 protrusion exhibited either a folded or an extended form, suggesting that CC1 works as an extending "arm". These findings provide clues to understand how dynactin binds to microtubules and regulates dynein.

Introduction

Dynactin is a multi-subunit complex that plays many essential roles in various cell functions, especially as an adaptor of dynein to vesicles or organelles (Kardon & Vale, 2009; Schroer, 2004). The importance of dynactin as a principal regulator of dynein and as an organizer of microtubule-based traffic is established but the molecular mechanisms of its diverse functions are not well known, mainly because of its very large and complicated architecture.

The dynactin complex is almost as large (~1.2 MDa) as cytoplasmic dynein and is composed of 11 different subunits (Schroer, 2004). This complex forms a unique asymmetric structure comprising two distinct domains, the Arp1 rod and the sidearm (Schroer, 2004). The Arp1 rod consists primarily of a polymer of Arp1 (Hodgkinson et al., 2005; Imai et al., 2006) and is responsible for cargo binding. One end of the rod (called the pointed-end) is capped by the "pointed-end complex" which consists of Arp11, p25, p27 and p62 (Eckley et al., 1999; Yeh et al., 2012; Yeh et al., 2013), whereas the other end (called the barbed-end) is capped by CapZ α/β (Schafer et al., 1994).

The sidearm is a thin elongated structure projecting from the barbed-end of the Arp1 rod. The main constituent of the sidearm is a dimer of p150^{Glued} (hereafter called p150), which is the largest subunit in dynactin and interacts with dynein (Karki & Holzbaur, 1995; Vaughan & Vallee, 1995). The two globular heads exist as the distal tip of the sidearm and are thought to be formed by the N-termini of the p150 dimer, including CAP-Gly and the basic-rich domains (Schafer et al., 1994). The CAP-Gly domain binds to microtubules (MTs) (Waterman-storer et al., 1995) and +TIPs (Steinmetz & Akhmanova, 2008), and particular mutations in this domain cause neuronal diseases (Farrer et al., 2009; Puls et al., 2003). The basic-rich domain directly alters the affinity of dynactin to MTs both *in vitro* and *in vivo* (Culver-Hanlon et al., 2006; Dixit et al., 2008; Kobayashi et al., 2017; Zhapparova et al., 2009). p150 is predicted to have a long (~330 aa) coiled-coil domain (CC1) almost immediately after the basic-rich domain and another coiled-coil (CC2; ~130 aa) on the C-terminal side.

The proximal end of the sidearm is called the "shoulder". This domain is considered to be composed of some part of p150, four copies of p50 (also called dynamitin) and two copies of p24 (Eckley et al., 1999). The shoulder is essential for tethering the sidearm to the Arp1 rod because overexpression of p50 disrupts the interaction between the sidearm and the rod (Echeverri et al., 1996; Jacquot et al., 2010; Melkonian et al., 2007).

Recently, a cryo-electron microscopy (EM) study (Urnavicius et al., 2015) revealed the detailed structure of the dynactin complex. The rigid backbone of the complex including the Arp1 rod and the shoulder domain was especially well resolved. In contrast, the distal part of the sidearm, corresponding to

p150, was only observed under conditions where p150 docked to the Arp1 rod. This configuration is markedly different from previously observed deep-etch rotary shadowing EM images of the dynactin complex (Schafer et al., 1994). In addition, p150 has scarcely been observed in other 2D or 3D averaged data of dynactin complex (Hodgkinson et al., 2005; Imai et al., 2006; Imai et al., 2014; Chowdhury et al., 2015). This elusiveness of p150 is likely derived from the flexible nature of the protein, which makes it difficult to properly understand the structure-function relationship of the dynactin complex, especially the mechanical basis for the dynamic interaction of dynactin with dynein and MTs.

CC1 is a particularly intriguing domain in p150 because it interacts with the dynein intermediate chain (IC) (King et al., 2003; Morgan et al., 2011). In mammalian cells, overexpression of CC1 disrupts the organizations of MTs and the Golgi complex, which are maintained by dynein force production (Quintyne et al., 1999). Thus, CC1 has been used widely as a dynein inhibitor *in vivo* and also in cell extract system (Ishihara et al., 2014; Suzuki et al., 2017). These inhibitory effects of CC1 on the cellular functions of dynein may arise from excess amounts of CC1 disrupting the formation of the dynein-dynactin complex. Interestingly, the results from *in vitro* assays remain controversial regarding the exact effect of CC1 on dynein motility because of conflicting observations: (i) the addition of CC1 to mammalian dynein severely impaired dynein affinity toward MTs and its processivity under some conditions even in the absence of the dynactin complex (Kobayashi et al., 2017; Tripathy et al., 2014); (ii) CC1 had no significant effect on mammalian dynein motility under other conditions (Ayloo et al., 2014; Culver-Hanlon et al., 2006); and (iii) CC1 enhanced the processivity of dynein in yeast (Kardon et al., 2009). Therefore, in an effort to comprehend these conflicting observations, it is important to determine the location and conformation of CC1 in the dynactin complex. CC1 was previously proposed to locate along the sidearm and the Arp1 rod (Schroer, 2004); however, recent cryo-EM data suggest that CC1 may extend from the head domain localizing at the distal end of the sidearm (Urnavicius et al., 2015).

Herein, we report the folding pattern and domain organization of p150 in a human recombinant dynactin complex by combining negative stain EM and nanogold labeling. Our "non-averaged" observations of individual molecules revealed that the sidearm was a remarkably flexible structure and adopted various morphologies. We determined the localization of CC1 and CC2 in the sidearm, under the condition that both domains did not dock to the Arp1 rod. In addition, the CC1 protrusion from the head domain was observed to exhibit two forms, a folded and an extended form, implying that CC1 undergoes a large conformational change. We propose a new model of the dynactin sidearm with the CC1 "arm" for dynein-binding, and discuss the regulatory role of CC1 for MT binding.

Results

EM images of the dynactin complex revealed the flexibility of an "undocked" sidearm

To obtain EM images of the dynactin complex, we exogenously expressed each of the dynactin recombinant subunits (p150, p62, p50 or p24) in HEK-293 cells. The subunit was fused with a streptavidin binding peptide (SBP)-tag for affinity purification and an octa-histidine tag (His-tag) for the localization study by nanogold labeling (**Fig. S1**). The streptavidin-based affinity purified proteins contained all the other subunit components of the dynactin complex (**Fig. S2**), indicating the effective formation of a complex of the exogenous subunit with the endogenous subunits in HEK-293 cells.

We firstly used recombinant p62 (SBP-p62 in **Fig. S1**), which locates at the pointed end of the Arp1 rod (Kitai et al., 2011; Schafer et al., 1994), in order to obtain an intact form of the dynactin sidearm. The negative stain EM images revealed the sidearm complex projecting from one end of the Arp1 rod (**Fig. 1A; Fig. S3A, left**). An overall configuration of the sidearm and the orientation of the projection were remarkably diverse, implying the flexible nature of the sidearm. Nevertheless, the sidearm exhibited common morphological features among molecules (**Fig. S3A, middle**) and, according to this, we divided the structure of the sidearm into three domains: two globular heads, a thin neck and a shoulder projecting from the barbed end of the Arp1 rod (**Fig. 1A, right**). Using these features as the common reference points (*e.g.*, the center of the head) (**Fig. S3A, middle and right**), we described the geometry of the sidearm (**Fig. 1B**), which suggested its preferable orientation and the range of motion.

Morphological characteristics of the sidearm were similar to those of native chick dynactin revealed by deep-etch rotary shadowing EM (Schafer et al., 1994) in its overall configuration and flexibility as well as in the size and appearance of each domain, indicating that our recombinant approach retains the structural integrity of the dynactin complex. In our setting, a "docked" form of the sidearm reported by cryo-EM (Urnavicius et al., 2015) was rarely observed (**Fig. 1A, panel *e*; Fig. 1B, purple and red**) and the majority of the molecules exhibited an "undocked" form, in which the sidearm did not dock to the Arp1 rod (**Fig. 1A, panels *a-d*; Fig. S3A, left; Fig. 1B, yellow and green**). We also found that glutaraldehyde fixation made the dynactin complex shrink. In this case, the undocked sidearm was rarely observed, and the neck domain and the head domain were hardly recognized as distinguishable structures probably because of cross-linking (**Fig. S3B, right**). Therefore, we focused on the structures of the undocked sidearm without fixation hereafter, and examined the domain organization and conformation of the sidearm which retains its flexibility.

Thin filamentous structure adjoining the head domain

Upon inspection of the head domain, we noticed that a thin filamentous structure adjoined the heads (**Fig. 1C, yellow arrows**; **Fig. S4A**). This structure was particularly subtle compared with other parts of the dynactin complex and its visibility was rather varied even in the same grid; the ratio of the dynactin complex with the thin filamentous structure in the well-stained region was 40-45% (N = 245, two independent experiments). The continuity between this structure and the two globular heads was not always distinct, possibly because of a particularly thin structure. Nonetheless, because it was found in almost every construct examined, we assumed that this filament invariably existed near all the heads but was not always visible by negative stain EM.

To investigate whether this filamentous structure is comprised of some dynactin-binding components or is a part of the dynactin subunits which have already known, we performed mass spectrometry-based proteome analysis of the purified sample. The results confirmed the presence of some proteins other than dynactin subunits. However, proteins known to bind to dynactin, including EB1, CLIP170, Bicaudal D and the dynein intermediate chain (Kardon & Vale, 2009), were not detected (**Table S1**). Thus, this filamentous structure appeared to be formed by a part of dynactin subunits within the sidearm protruding from or associated with the head domain (**Fig. 1C, right**). The distance between the tip of the filament/protrusion and the center of the head was 28.8 ± 4.1 nm (mean ± SD, N = 20) and summarized with "somatometry" of the dynactin complex in **Fig. S4B**.

Localization of the N- and C-termini of the p150 subunit

To dissect the molecular architecture of the dynactin sidearm, we made a series of His-tagged mutants of p150 (**Fig. S1**) and labeled the tagged site in the dynactin complex with gold nanoparticles modified with Ni-NTA (see materials and methods). The efficiency and specificity of nanogold labeling of the human dynactin used in this study has been reported previously (Kitai et al., 2011). The nanogold labeling of p150-N-His revealed that the N-terminus of p150 was localized around the heads (**Fig. 2A**). By setting an origin at the center of the heads, the position (the distance from the origin and the angle from the neck direction) of the center of each gold nanoparticle was measured (**Fig. 2B**). Although the position of each gold nanoparticle was widely scattered, the centroid of the gold nanoparticles was located close to the center of the heads. For p150-C-His, the gold nanoparticles were found around the shoulder (**Fig. 2C**) and therefore we set the origin at the barbed end of the Arp1 rod. The centroid of the C-terminus of p150 was in the middle of the shoulder and the position of each gold particle was also scattered (**Fig. 2D**). The location of the N-terminus is consistent with a previous model (Schroer, 2004). In contrast, the location of the C-terminus does not agree with the model where the C-terminus of p150 extends along the Arp1 rod

(Schroer, 2004) but agrees well with the recently reported structure of the dynactin complex (Urnavicius et al., 2015).

The thin filamentous structure is formed by CC1 of p150 protruding from the head

The observation of the thin filamentous structure and nanogold labeling results of both termini of p150 raised the possibility that the thin filamentous structure is an essential component of the sidearm and is formed by a part of p150. Therefore, we next focused on the folding pattern of p150. p150 is a large protein (~1250 aa) predicted to form two long coiled-coil structures (CC1 ~50 nm, CC2 ~20 nm). We further divided CC1 into CC1a and CC1b at the hinge point, where its coiled-coil structure is supposed to be disrupted (**Fig. 3A**). Based on the nanogold labeling results of both termini of p150 and predicted coiled-coil lengths, we considered that p150 must fold back at some point. Thus, we propose two models: (i) the N-terminal folded model, in which p150 folds back at the hinge between CC1a and CC1b (**Fig. 3B**, **left**); and (ii) the C-terminal folded model, where CC1 folds back at the region between CC1b and CC2 (**Fig. 3B**, **right**). The N-terminal folded model explains the filamentous structure described above as CC1 protruding from the head domain.

To test these models, the His-tag was inserted at three sites: the N-terminal end of CC1 (CC1-start); the hinge point, which lies between CC1a and CC1b (CC1-hinge); and the C-terminal end of CC1 (CC1-end) (**Fig. 3A**). The nanogold labeling experiments showed that CC1-start and CC1-end were located on the heads (**Fig. 3C, top and bottom**). In molecules which distinctly exhibited the thin filamentous structure (**Fig. 3C**, yellow arrows), the gold nanoparticles were located close to the junctions of the heads and the filament in these two constructs. In contrast, for the CC1-hinge, the gold nanoparticles were observed at the tip of the filament (**Fig. 3C, middle**). Distributions of the gold nanoparticles labeling the CC1-start and those labeling the CC1-end were almost the same and centralized around the head. The CC1-hinge exhibited a broader distribution than the two others (**Fig. 3D, top**). The distance from the center of the heads to the gold nanoparticles of the CC1-start and CC1-end were 10.0 ± 4.0 nm and 7.9 ± 3.3 nm, respectively, whereas the CC1-hinge was located further away from the heads (22.2 ± 3.3 nm) (**Fig. 3D, bottom left**). These results mean that both CC1a and CC1b lie between the heads and the tip of the filament, and strongly indicate that CC1 folds back at the hinge and are consistent with the N-terminal folded model (**Fig. 3B**, **left**).

We subsequently made a CC1-deletion mutant of p150 (p150 ΔCC1 in **Fig. S1**). The purified p150 ΔCC1 showed a p150 band with higher electrophoretic mobility in SDS-PAGE (**Fig. S2C**), indicating that virtually all dynactin contains a homodimer of CC1-deleted p150. In the EM images, p150 ΔCC1 exhibited

a similar configuration as SBP-p62, which has wild-type p150 (**Fig. 3E and Fig. S4C**). The lengths of the shoulder and the neck were almost the same between ΔCC1 and wild-type p150 (**Fig. 3F and Fig. S4B**). Based on the deletion and nanogold labeling of CC1, we concluded that the thin filamentous structure was an essential component of the dynactin sidearm protruding from the head and it was formed by CC1 of p150 folding back at the hinge.

The neck domain is formed by CC2 of p150

Because CC1 does not form the neck domain, CC2 or its nearby regions were considered as candidates for the neck domain. CC2 is ~130 aa in length and flanked by a helix-rich region (HR-region) and a C-terminal region (C-region) (**Fig. 3A**). The HR-region spans the region between CC1 and CC2, contains ~ 370 aa and is predicted to be rich in α-helix (McGuffin et al., 2000) (See **Fig. S7A**). Using the same strategy as for CC1, His-tagged mutants for labeling CC2 (CC2-start-His and CC2-end-His) and a CC2-deletion mutant (p150 ΔCC2) were prepared (**Fig. S1**). Nanogold labeling experiments showed that the CC2-start was localized at the head domain (**Fig. 4, A and B**) and the CC2-end at the junction of the neck domain and the shoulder domain (base of neck) (**Fig. 4, C and D**). Because it was difficult to measure the distance and angle of the gold nanoparticle from the base of neck, we set the origin at the barbed end of Arp1 rod and compared the position of the gold nanoparticle to the base of neck (**Fig. 4D**). In addition, p150 ΔCC2 exhibited neck-lacking morphology, where the head and the shoulder were in close proximity, although the protrusion formed by CC1 at the distal end of the sidearm was still evident (**Fig. 4E**). These results demonstrated that CC2 was the neck itself.

C-region of p150 forms a part of the shoulder domain and is indispensable for the complex assembly

The shoulder domain is thought to consist of p150, p50, and p24 subunits (Eckley et al., 1999). Our results demonstrated that the C-terminus of p150 located at the middle of the shoulder (**Fig. 2D**) and the CC2-end at the base of neck (**Fig. 4D**), which indicates that C-region of p150 (**Fig. 3A**) resides in the distal part of the shoulder. This new p150 model implies that the contribution of p150 to the total mass of the shoulder domain could be considerably less than previously expected (Schroer, 2004). To clarify the molecular arrangement of the shoulder domain, we firstly localized p50 and p24 by nanogold labeling and then examined the role of the C-region of p150 by deletion analysis.

The His-tag at the N-termini of p50 (p50-N-His) and p24 (p24-N-His) (**Fig. S1**) were labeled and found to be localized close to the barbed end of the Arp1 rod (**Fig. 5A, upper**). The gold nanoparticles of the both mutants exhibited similar distributions (**Fig. 5B**). Their distances from the barbed end were 7.8 ± 4.1

nm (p24-N-His) and 9.3 ± 4.5 nm (p50-N-His), respectively, which were significantly smaller than that of p150-C-His (15.2 ± 7.3 nm) (mean ± SD, $p < 0.0001$ in Welch's t-test) (**Fig. 2D and Table S2**).

The mutants with the His-tag at the C-terminus (p50-C-His and p24-C-His) were purified as complexes (**Fig. S2C**). For p50-C-His, the gold nanoparticles bound over a very broad area of the sidearm from the shoulder to the head, but were not found along the Arp1 rod (**Fig. 5A, lower**). Furthermore we often observed an extraordinary form of the sidearm in this mutant (**Fig. S5A**). Since overexpression of p50 disrupts the sidearm from binding to the Arp1 rod (Echeverri et al, 1996), we postulated that the C-terminus of p50 is important for proper sidearm formation. The observed broad distribution of the gold nanoparticles might have resulted from the loss of sidearm integrity. In contrast, p24-C-His exhibited typical morphology of sidearm, but showed no specific nanogold labeling (data not shown). This may arise from the C-terminus of p24 being buried and thus the gold nanoparticles cannot access the His-tag. When we placed the His-tag after the SBP sequence of p24-C-His, the purified complex was labeled with the gold nanoparticles around the barbed end (**Fig. S5B**). However, the position of the gold particles less accurately defined the position of the C-terminus of p24 because of the insertion of SBP between the C-terminus and the His-tag. The results of the nanogold labeling experiments suggest that p50 is situated in the shoulder domain and the C-terminal side of p50 might be associated with the C-region of p150, tethering it to the upper part of the shoulder.

We prepared C-terminal truncation mutants of p150 to clarify the role of the C-region of p150 in the formation of the dynactin complex. When the C-region was truncated (p150 CC2-stop in **Fig. S1**), neither Arp1 nor p50 was co-purified with this mutant (**Fig. S2C**), indicating that the C-region is essential for incorporation of p150 into the dynactin complex. We observed the purified p150 CC2-stop by EM and confirmed that no Arp1 rod was present. Instead, a distal part of the sidearm, in which the shoulder domain was absent, was observed (**Fig. 5C**). In this truncated form of p150, three domains were discernible: two globular heads, the neck and the protrusion formed by CC1. As with the sidearm within the dynactin complex (**Fig. 1A**), the CC1 protrusion (**Fig. 5C, yellow arrows**) was thicker and longer than the neck formed by CC2 (**Fig. 5C, light blue arrows**), and these two filaments protruded from the heads in the opposite direction. These results demonstrated that the C-region of p150 constitutes a part of the shoulder domain and is indispensable for p150 incorporation into the dynactin complex via the remaining part of the shoulder composed of p50/p24. This conclusion agrees with the recent cryo-EM study that revealed that three α-helices, assigned as the p150 C-terminus, p50 and p24, were bundled in the shoulder (Urnavicius et al., 2015). Our observation that p50-C-His disrupted the structural integrity of the shoulder (**Fig. S5A**) suggests that the C-terminus of p50 is a candidate for the dimerization domain of p50/p24

heterotrimers within the shoulder (Urnavicius et al., 2015). Additionally, the result that the truncation of the p150 C-region disrupts the incorporation of p150 into the complex (**Fig. 5C**) may explain the rough eye phenotype of the *Glued*[1] mutation found in fruit flies (McGrail et al., 1995; Fan and Ready, 1997) as a partial or total loss of complex integrity, because transcription of p150 in *Glued*[1] is terminated in the middle of CC2 (Swaroop et al., 1985).

We found an additional evidence for further studying the incorporation of p150 into the dynactin complex. Since p150 is more abundant than other components in cells exogenously expressing recombinant p150, some p150 molecules are postulated to exist as isolated p150 dimers. Thus, there must be two types of p150 molecules: those that are incorporated into the dynactin complex and those that are not incorporated. In SDS-PAGE, the intensity of the p150 band in the mutants expressing recombinant p150 was higher than that in SBP-p62 (**Fig. S2C**). We certainly found that, in the preparation of p150 mutants, isolated forms of p150 dimers were frequently observed with the whole dynactin complex, and these two kinds of particles were distinguishable in negative stain EM images (**Fig. 5D, left**). The isolated forms of p150 dimers had two oval structures at one end of the neck and the two globular heads with the CC1 protrusion at the other end (**Fig. 5D, right**). Compared to the EM images of p150 CC2-stop (**Fig. 5C**), the two oval structures were conspicuous. We considered that this domain was likely to be composed of the C-region of p150 or perhaps might also include p50/p24. Together with the deletion analysis of the C-region of p150, our results demonstrated that these two oval structures were an essential domain for forming the shoulder domain and completing the dynactin complex formation with the Arp1 rod.

We also observed that gold nanoparticles bound to the His-tagged site of the isolated p150 dimer of each mutant (**Fig. 5E, red arrow heads**). The position of the gold nanoparticles bound to CC1-end-His was at the proximal end of the protrusion, and that of CC2-end-His was at the proximal end of the neck, coinciding with the results of the complex (**Fig. 3C and Fig. 4C**). Gold nanoparticles bound to the C-termini of the isolated p150 dimers (p150-C-His) were scattered around the oval structure and their positions could not be further specified.

In the EM images of the whole dynactin complex, the most distal part of the shoulder was slightly swollen and divided into two smaller buds, which now we interpreted as the C-regions of p150. Based on these observations and the nanogold labeling of p150-C-His (**Fig. 2, C and D**), we presume that a dimer of p150 is situated in the dynactin complex as indicated in **Fig. 5F**.

We labeled all peptides that constitute the dynactin sidearm, i.e., p24, p50 and p150, with gold nanoparticles. The distributions of these labeled peptides from the barbed end of the Arp1 rod are present in **Fig. S6A**. This graph indicates both a movable range of the sidearm and a positional relationship among

specific sites or subunits in the sidearm. Importantly, the results clearly demonstrated that p150-C was more distal from the Arp1 rod than p50-N and p24-N, and the radial distribution of p150-C was broader than that of p50-N and p24-N. Two-dimensional standard deviations of the nanogold labeling showed the dispersion around the centroids, thus revealing the partly overlapping but distinct distributions of p150-C and p50-N (**Fig. S6B**). These map overlays of the labeled sites in the sidearm provide further support for our model in which p50/p24 constitutes the proximal side of the shoulder and p150 constitutes the remaining distal part of the sidearm (**Fig. 5F**).

Detailed structure of the head domain

We have already identified three regions in p150 as the structural domains in the sidearm: the CC1 as the protrusion from the head (**Fig. 3**), the CC2 as the neck (**Fig. 4**) and the C-region as the distal side of the shoulder (**Fig. 5**). The remaining unidentified regions in p150 are N-terminal region (N-region, including the CAP-Gly domain) and the HR region, which lies between CC1 and CC2. When translation of p150 was terminated at the end of the HR region (HR-stop in **Fig. S1** and **Fig. S2C)**, the molecule with the two heads and the CC1 protrusion was observed, as expected (**Fig. S7B**). However, the relationship between the observed heads and the two regions in p150 (the N-region and the HR region) remained unclear. Therefore, we next examined the structural roles of the N-region and the HR region, questioning the detailed composition of the head domain.

We made deletion mutants lacking the entire or a part of the HR-region (**Fig. S1 and Fig. S7A**). In the mutant lacking the entire HR region (p150 ΔHR), the head domain was almost never observed and the outline of the complex distal to the shoulder domain was quite obscure (**Fig. 6A**, **left; Fig. S7C**). For mutants lacking the former or the latter half of the region (p150 ΔHR-a and p150 ΔHR-b, respectively, **Fig. 6A, middle and right**), the head domains were more distinct than those of p150 ΔHR, but their head sizes appeared to be slightly smaller than that of the wild-type p150 (**Fig. 1A, C and Fig. S4A**). In all of three HR deletion mutants, the sidearm structure below the head domain, namely the neck and shoulder, remained unchanged compared with the wild-type sidearm. In contrast, the CC1 protrusion was not distinctly observed except for p150 ΔHR-b (**Fig. 6A**, yellow arrows). These results indicated that the HR-region is a part of the head domain and the former half of the region (HR-a) is important for the structural integrity of CC1.

The observation that the HR-region constituted the heads of dynactin together with the N-region led us to question what the relative contribution of each region was to the head domain. p135 is a splicing isoform of p150 expressed in mammalian neurons that lacks most of the N-region (Dixit et al., 2008; Tokito et al.,

1996). Thus, we made two N-region deletion mutants: one mimicking p135 (p135) and the other lacking the entire N-region and starting at CC1 (p150 ΔN) (**Fig. S1 and Fig. S2C**). Intriguingly, the morphology of these two mutants did not differ from that of the full length p150 and the sizes of the heads were indistinguishable from that of p150 (**Fig. 6B**, pink arrows). Furthermore, the CC1 protrusions of both p135 and p150 ΔN were observed to be similar to that of wild-type p150 (**Fig. 6B**, yellow arrows). These results suggest that the contribution of the N-region to the size of the head domain may be considerably small when compared with that of the HR-region.

The CC1 protrusion adopts folded and extended forms

We have already demonstrated that the HR-region is an essential constituent of the head domain (**Fig. 6**) and the N-region is located around the HR-region (**Fig. 2, A and B**). However, how these two domains are structurally linked remains unclear because the size of the N-region (~ 190 aa) is small for EM observation. CC1 lies between these two domains and the CC1 protrusion was occasionally observed to be more extended (**Fig. 7A**) when compared with the ~ 30 nm protrusion (**Fig. S4, A and B**). Here, the extended form was measured as being more than 50 nm in some molecules; however, the precise measurement was difficult because of the small size of the N-region in wild-type p150. GFP was fused to the N-terminus of p150 (p150-N-GFP in **Fig. S1 and Fig. S2C**) in an attempt to visualize the N-region, i.e., we expected that the mass of GFP + N-region (GFP-N) was sufficiently large for EM observation. We indeed observed that GFP-N (~ 490 aa) was as large as the HR-region (HR, ~ 470 aa) and both domains exhibited similar globular structures. We observed that the distance between GFP-N and HR was varied noticeably with GFP-N located in close proximity of or distal from HR (**Fig. 7, B and C**). In the former case, the head domain in the p150-N-GFP was larger than the other mutants examined (**Fig. 7B**). HR and GFP-N were situated at the base of the CC1 protrusion and were in contact with each other in some molecules (**Fig. 7B, middle and right**) and not in contact in other molecules (**Fig. 7B, left**). The observed sizes of HR and GFP-N were similar, which made it difficult to distinguish between the two by visual inspection.

In the latter case (**Fig. 7C**), however, GFP-N was observed as a separate and distinct domain from the HR, with these two domains bridged by a hooked CC1. This finding indicates that CC1 adopts not only a folded form, which was reported in this and previous studies, but also an extended form, which was observed here for the first time. The co-existence of both forms of CC1 in a single sample suggests that CC1 undergoes a conformational change between the two forms. It is likely that CC1a and CC1b contact each other and form a supercoil in the folded form, whereas they exist as two separate coiled-coils in the extended form. In line with this, the CC1 protrusion was thinner in the extended form (**Fig. 7C**) than in

the folded form (**Fig. 7B**). Varying visibility of the CC1 protrusion described above (**Fig. 1, A and C**) may have been affected by this thinner form of CC, i.e., the extended form of CC1 may be more difficult to detect by EM than the folded form. Furthermore, owing to the GFP fusion, we also found that the two N-regions within the p150 dimer in the extended form were able to separate from each other (**Fig. 7C, middle and right**).

Based on our GFP fusion, together with nanogold labeling and deletion analysis of the p150 mutants, we present a new model for the domain organization of p150 and how it is situated in the dynactin complex via p50/p24 (**Fig. 7D**). Since CC1 adopted either the folded or extended forms, we propose that CC1 acts like an "arm", which undergoes a large conformational change (CC1-folded and CC1-extended in **Fig. 7D**).

Discussion

Identification of p150 domains and overall structure of the dynactin complex

In this study, we investigated into the molecular architecture of the dynactin complex by EM observation. Dynactin is a large and complicated protein complex, and what makes dynactin unique among other large protein structures is its asymmetry and flexibility. Whereas the length and thickness of the Arp1 rod is fairly constant, the orientation and configuration of the sidearm is remarkably diverse (**Fig. 1**). This explains why the Arp1 rod and the shoulder part of the sidearm is visible but the distal part of sidearm is normally invisible in EM class averages of the dynactin complex (Imai et al., 2006; Imai et al., 2014; Chowdhury et al., 2015). However, functionally intriguing domains of the sidearm, such as MT-binding and dynein-binding domains, lie in this invisible or "hard to be averaged" part.

We utilized nanogold labeling and truncated mutants of the human dynactin complex and revealed how p150 was folded and located within the distal side of the sidearm, through EM observation of individual molecules without averaging procedure. Importantly, we localized two coiled-coils (CC1 and CC2) and N-region of p150. CC1 is widely accepted to bind with the dynein IC (King et al., 2003; Morgan et al., 2011) and the N-region with MTs (King & Schroer, 2000; Waterman-Storer et al., 1995). Identification of CC1 as the protrusion from the head domain (**Fig. 3**) indicates that the binding sites for dynein or MTs are located farther apart from the Arp1 rod than previously understood (Schroer, 2004). CC2 was identified as the neck domain, which was situated in the middle of the sidearm (**Fig. 4**). The proximal end of the neck is highly flexible and likely to serve as the joint of the sidearm (**Fig. 1B and Fig. S6A**). Furthermore, it is noteworthy that CC1 was found to adopt the extended and folded forms (**Fig. 7**). The conformational change between the two forms adds another morphological variation to the sidearm, which might facilitate its interaction with dynein and MTs.

Labeling of flexible objects by gold nanoparticles

Visualization of specific components within biological macromolecules by nanogold labeling has been one of the powerful applications of electron microscopy. Especially, chemically modified gold particles have been recently used to specifically label genetically modified tagged proteins (Guesdon et al., 2016; Song et al., 2014). We have developed Ni-NTA-gold nanoparticles with diameter less than 5 nm for localizing the specific subunits or domains within large protein complexes (Kitai et al., 2011). We previously applied it to light chain 1 in axonemal dynein (Ichikawa et al., 2015) and p62 in the pointed end of the dynactin Arp1 rod (Kitai et al., 2011).

In the present study, our targets were the components of the sidearm and we found that nanometer scale

localization by Ni-NTA-gold nanoparticles also worked well for this highly flexible and elongated object. In particular, specific sites within ~30 nm CC1-protrusion (**Fig. 3**) and ~20 nm CC2-neck (**Fig. 4**) were clearly discernible by our labeling method since the total length of the sidearm was as long as 90 nm (**Fig. 1B and Fig. S4B**). This enabled us to determine the folding pattern and the domain organization of p150 in the sidearm without compromising its flexibility and dynamics. We labeled numerous sites along the sidearm with nanogold particles (**Fig. S6A**). These distributions probably reflected the dynamics of the sidearm, and were consistent with the measurement of the position of the head and the base of neck without labeling (**Fig. 1B, lower**).

The difference of distribution ranges of labeled gold nanoparticles among the constructs may also reflect whether the peptide chain in the vicinity of the labeled site was flexible or rigid. For example, the distribution ranges were wide for p150-N-His and p150-C-His, narrow for p150 CC2-start-His, and intermediate for p50-N-His (**Fig. S6B**). The observed wide distribution of the N-terminus of p150 was consistent with the newly discovered conformational change of the CC1 protrusion (**Fig. 7**) and with the previous report that N-terminal 25 amino acids were not included in the crystal structure (Weisbrich et al., 2007) presumably because this region is unstructured. Therefore, we assume that the observed distribution of gold nanoparticles reflects the nature of the protein structure and it enabled us to get insight into the dynamic property of the protein.

Observation of CC1 protrusion and comparison with cryo-EM structure

We observed a protrusion from the head, which was identified as CC1, but it was not always visible. This structure was not observed in previous reports of negative stain EM images of dynactin complex (Imai et al., 2006; Imai et al., 2014). It should be noted that this protrusion has been observed in the already published deep-etch rotary shadowed images (the left and right pictures of the top 3 rows in Figure 3 of Schafer et al., 1994). Part of the protrusion was also visible in some class averages of the recently reported cryo-EM image of the dynactin complex and it was identified as CC1 by its length (Urnavicius et al., 2015). We labeled three characteristic sites in CC1 (CC1-start, CC1-hinge and CC1-end) with gold nanoparticles and made the CC1 deleted mutant (ΔCC1) to directly demonstrate that the CC1 domain constitute the protrusion from the head (**Fig. 3**). In our observation of individual molecules, each of the domains that constitute the distal end of the sidearm (the head, the neck and the CC1 protrusion) were conspicuous and distinguishable, and provided a structural signature to map the gold nanoparticles binding to p150 (**Fig. 3 and Fig. 4**). As described above, the part of the sidearm distal to the shoulder, corresponding to p150, was extremely flexible and adopted various conformations. This flexibility

prohibited us from averaging p150.

The protrusion formed by CC1 adopted a wide range of orientations with respect to the neck direction (**Fig. 3, C and D**) and adopted two categories: folded and extended forms (**Fig. 7**). In marked contrast, the distal part of the sidearm including the CC1 protrusion docked to the Arp1 rod in the class average of cryo-EM (Urnavicius et al., 2015). We found that, under our conditions, the vast majority of the sidearm population was in the undocked form with the occasional observation of molecules in the docked form (**Fig. 1, A and B**). In addition, when the dynactin complex was fixed with glutaraldehyde, the complex shrunk and the docked form was preferred probably because of cross-linking (**Fig. S3B**). The undocked sidearm was flexible and exhibited diverse structures (**Fig. 1B, yellow and green; Fig. S3A**), whereas the docked sidearm exhibited a uniform structure (**Fig. 1B, purple and red; Fig. S3B**), which might be suited for producing class averages of the sidearm structure. An intriguing question to be addressed is whether dynactin in the cell adopts both the docked and undocked forms to play distinct physiological roles.

The CC1 protrusion as a possible regulator for interaction with dynein and MT

There are some descriptions of the dynein-binding region within the CC1 region (Siglin et al., 2013; Tripathy et al., 2014). Moreover, CC1-binding with dynein was shown to have positive and negative effects on dynein motility, depending on the length of the fragment or the existence of adjacent domains (Kobayashi et al., 2017; Tripathy et al., 2014). As described in Introduction, contrary to the well-known inhibitory effect of the CC1 fragment on dynein function *in vivo*, its mechanism of action and *in vitro* effect on dynein motility remains controversial. In this study, we found that CC1 folded back at the CC1-hinge (**Fig. 3**), and that CC1a and CC1b had contact with each other (folded form) or separated (extended form) (**Fig. 7**). We speculate that the affinity of CC1 toward dynein IC and its apparently ambiguous effect on dynein motility are regulated by the conformational change of the CC1 protrusion. For example, an intramolecular interaction between CC1a and CC1b may regulate its effect on dynein, as proposed in the previous study (Tripathy et al., 2014).

The N-terminal region is an indispensable portion of p150 for microtubule binding, and the affinity of dynactin toward MTs is intricately controlled by CAP-Gly domain and both N- and C-terminal basic rich extensions (Culver-Hanlon et al., 2006; Dixit et al., 2008; Wang et al., 2014). It was previously proposed that 'the head' of dynactin seen in EM was the N-region (Schroer, 2004). However, deletion mutants in this study revealed that the HR-region constituted the main part of the dynactin head (**Fig. 6A**) and N-region was considerably smaller than the HR-region (**Fig. 6B**). Furthermore, we found that the N-region

located very close to the head in some molecules while detached from the head in other molecules (**Fig. 3** and **Fig. 7**). The result that the head domain is mainly composed of the HR-region is consistent with the averaged image obtained by cryo-EM (Urnavicius et al., 2015), although the N-region disappeared in those cryo-EM images probably because their sample consisted mainly of p135 isoform and lacked the N-region (See **Fig. 6B** for comparison).

In mammalian cells, the MT binding property of the dynactin is controlled by expression of several isoforms in which the N-region is partially truncated or rearranged through alternative splicing (Dixit et al., 2008; Zhapparova et al., 2009). The p150 constructs used in this study (p150-B or DCTN1B) lacked exon 5–7 (basic-rich domain). We examined previously MT-binding ability of this isoform by TIRF microscopy and found that isolated p150-B rarely bound to MTs *in vitro* but deletion of CC1 domain remarkably restored the intrinsic MT-binding ability of CAP-Gly (Kobayashi et al., 2006; Kobayashi et al., 2017). The structural characteristics and the conformational change of the CC1 protrusion revealed by the present study offer a simple explanation for the phenomenon. Here, most of the N-region including CAP-Gly is usually masked by the folded form of CC1 and this state inhibits the binding of the N-region to MTs; however, if the whole CC1 domain is deleted or CC1 is turned into the extended form, the N-region is un-masked and binds to MTs (**Fig. 7E**). We note that one of the neuronal isoforms containing both CAP-Gly and basic-rich domain (p150-A or DCTN1A) binds to MTs *in vitro* (Culver-Hanlon et al., 2006; Kobayashi et al., 2017; Miura et al., 2010). Thus the basic-rich domain presumably evades this auto-inhibitory regulation of the CC1 protrusion.

Previous studies showed that the interaction between CAP-Gly and MTs was not always required for processive movement of dynein (Kardon et al., 2009) but was necessary for the initiation of dynein-driven retrograde transport of vesicles from the neurite tip (Lloyd et al., 2012; Moughamian et al., 2012) and for the initiation of ultra-processive movement of DDB (dynein, dynactin and BICD2) complex at tyrosinated MTs (McKenney et al., 2016). Regulation of CAP-Gly by the CC1 protrusion may be important for understanding these differential effects of CAP-Gly on MT-based transport. In another cellular context, the inhibition of the direct interaction of dynactin with MTs may play a key role in a passive transportation of dynein to the MT plus ends by plus end tracking proteins (+TIPs) (Akhmanova and Steinmetz, 2008). Recent *in vitro* reconstitution assays of MT plus end tracking system have shown that recruitment of dynein to MT plus end was mediated by a p150 fragment including CAP-Gly and CC1 (Duellberg et al., 2014) or dynactin complex (Baumbach et al., 2017; Jha et al., 2017). These studies reported that the plus end tracking of dynein was hierarchically controlled by +TIPs and dynactin, and tuned by additional factors, such as BICD2 or Lis1. It is important to re-examine these elaborate regulations of dynein motility

by dynactin in the light of the conformational change of CC1.

In conclusion, this study revealed the overall shape of the dynactin sidearm including the protrusion from the head domain. We identified the protrusion as the CC1 and deciphered the folding pattern of p150. The dynactin sidearm was depicted as an enormously elongated sub-complex with distinct domains (**Fig. 7D**). Our findings characterized the sidearm as a flexible arm for encountering and binding to dynein and/or MTs, which must be essential for the role of dynactin as the largest regulator of MT-based traffic. Furthermore, the observed conformational change of the CC1 protrusion within the sidearm may also be important for controlling the interaction of dynactin with dynein and MTs. These data were obtained by the close observation of individual dynactin molecules with diverse morphologies, which probably reflected the dynamics of the protein. Our EM data and proposed model provide the mechanical basis for elucidating the intricate regulatory role allocated to the sidearm and we believe it will lead to a deeper understanding of the structure-function relationship of dynactin in the cell.

Materials and methods

Construction of expression vectors

cDNAs encoding the dynactin subunits were amplified from HEK-293 cells by RT-PCR. The PCR primers used for cloning of dynactin subunits are as follows: 5'-ATGGCACAGAGCAAGAGGCAC-3' and 5'-TTAGGAGATGAGGCGACTGTG-3' for p150 (DCTN1, NM_004082), 5'-ATGGCGTCCTTGCTGCAGTCG-3' and 5'-TTAAGGAAGAAGTGGGCCCAA-3' for p62 (DYNC4, NM_001135643), 5'-ATGGCGGACCCTAAATACGCC-3' and 5'-TCACTTTCCCAGCTTCTTCAT-3' for p50 (DCTN2, NM_006400), and 5'-ATGGCGGGTCTGACTGACTTG-3' and 5'-TCACTCCTCTGCTGGCTTCAC-3' for p24 (DCTN3, NM_007234). Note that our cloned dynactin sample of p150 from HEK-293 cells was DCTN1B isoform, which lacked some amino acids of the basic-rich domain (Δexon 5-7) as reported (Dixit et al, 2008 and Zhapparova et al, 2009). We found a missense mutation (c.2566G>C) which produces p.A856T in the HR region; however, we confirmed that the mutation does not affect the dynactin structure. The primers used for construction of p150 mutants are summarized in **Table S3**. For p135 construction, N-terminal 131 amino acids were deleted and 17 amino acids were added to its N-terminus to mimic p135 isoform found in neuron (Tokito et al, 1996).

The PCR products were cloned into pcDNA5/FRT/TO (LifeTechnologies, Carlsbad, California), a tetracycline-inducible mammalian expression vector. For protein purification, the streptavidin-binding peptide (SBP) tag was fused at either the N- or C-terminus of the dynactin subunits. For Ni-NTA Au nanoparticle labeling, an octa-histidine tag (His-tag) was inserted in either the N- or C-terminus or internally through a short linker (Gly-Gly-Gly-Ser) (see **Fig. S1**). The mutant p150-N-GFP (**Fig. S1**) has GFP fused at N-terminus of p150 as previously described (Kobayashi et al., 2017). A His-tag and SBP tag were included in the GFP and used for purification (Kobayashi et al., 2008). The insertion of these tags or deletion of specific domains was achieved by inverse PCR.

Generation of the stable inducible HEK-293 cell lines

Flp-In T-REx HEK-293 cells (LifeTechnologies) were maintained in Dulbecco's modified Eagle's media (DMEM, LifeTechnologies) supplemented with 10% fetal calf serum and 2 mM L-glutamine. The stable inducible cell lines were generated by co-transfection of the pcDNA5/FRT/TO vector containing recombinant dynactin subunits with the pOG44 vector encoding Flp recombinase according to the manufacturer's instructions. The transfectants were screened by including 100 μg/ml hygromycin and the hygromycin-resistant colonies were harvested.

Purification of the dynactin complex

Purification of the dynactin complex was carried out using a SBP-tag (Ichikawa et al, 2011; Kobayashi and Murayama 2009). Stable HEK-293 cells were cultured in five 150-mm tissue culture dishes and protein expression was induced by doxycycline (2 μg/ml) for 48 h. Cells were harvested, washed twice with phosphate buffered saline, and homogenized in buffer A (50 mM Tris-HCl, pH 7.5, 0.15 M NaCl, 10% sucrose, 5 mM MgSO4, and 1 mM dithiothreitol) containing 0.5 mM ATP, 0.05% Triton X-100, and complete mini protease inhibitor cocktail (Roche, Basel, Switzerland). The lysate was centrifuged and the resultant supernatant was applied onto a StrepTrap HP column (1 ml) (GE Healthcare, Chicago, Illinois) pre-equilibrated with buffer A. After extensive washing of the column with buffer A, the bound proteins were eluted in buffer A containing 2.5 mM desthiobiotin. The fraction from the peak of interest was quickly frozen in liquid nitrogen and stored at -80 °C until use for EM observation.

Mass spectrometric analysis to identify proteins

Peptide mapping was carried out using the Triple TOF 5600 mass spectrometer systems, which consisted of nano-ESI and TOF (AB SCIEX MA, USA). The Triple TOF 5600 mass spectrometer was combined with Eksigent NanoLC-Ultra system plus cHiPLC-nanoflex system (AB SCIEX MA, Framingham, Massachusetts) with attached 75 μm (id) × 15 cm Chrom XP C18-CL column. The solvent system consisted of (A) 0.1% formic acid/2% acetonitrile and (B) 0.1% formic acid/90% acetonitrile. The solvent was linearly changed from 2% B to 40% B for 40 min and subsequently fixed at 90% B for 5 min. The flow rate was 300 nl/min. Identification of proteins was performed using Protein Pilot 4.0 software (AB SCIEX MA) (Hayashi et al., 2013).

The proteins were subjected to digestion as described previously (Fujimura et al., 2008). Finally, the residue was dissolved in 30 μl of 0.1% formic acid. Aliquots were used for peptide identification by mass spectrometry.

Negative stain electron microscopy and nanogold labeling

Samples were applied to pre-hydrolyzed carbon-coated EM grids and negatively stained with 1.4% (w/v) uranyl acetate solution, observed at 40,000× magnification in a transmission electron microscope, H7500 (Hitachi High-Techonologies, Tokyo, Japan) operating at 80 kV. Micrographs were taken using a 1024 × 1024 pixel CCD camera, Fast Scan-F114 (TVIPS, Gauting, Germany). The nominal magnification was 40,000×, giving a sampling of 2.6 Å/pixel. The images were not inversed for the figure presentation.

Ni-NTA-gold nanoparticles were synthesized according to Kitai et al, 2011 using a modified method to

reduce the diameter to 3 nm. The purified proteins were mixed with Ni-NTA-gold nanoparticles and incubated on ice for 30 min. The dynactin complex and Ni-NTA-gold nanoparticles was mixed to yield 10–20% labeled particles for all samples examined. These conditions were chosen to avoid non-specific binding of Ni-NTA Au nanoparticles. It is noted that the free Ni-NTA-gold nanoparticles rarely bound to the carbon surface of the grid, probably because of an electrostatic repulsion.

The length and angle in the EM images were measured using ImageJ software (NIH). Reference points of dynactin (**Fig. S3A**) and the center of the gold nanoparticles were determined by visual inspection. We used two different polar coordinates to measure and map these points (**Fig. S3A, right**). For the gold nanoparticles bound around the head of dynactin (**Figs. 1D, 2D and 3B**), the distance from the origin (X: the center of the heads) and the angle from the neck direction (XY) were measured and mapped as shown in **Fig. S3A, right, red graph**. For the gold nanoparticles bound along the shoulder of dynactin (**Figs. 1F, 3D and 4B**) and for the points within the sidearm (**Fig. 1B**), the distance from the origin (P: the barbed-end of the Arp1 rod) and the angle from the Arp1 rod direction (PQ) were measured and mapped as shown in **Fig. S3A, right, blue graph**.

Acknowledgments

This work was supported by JSPS KAKENHI Grant Numbers 25117503 and 25291031(to Y.Y.T.), 24590330 (to T.M.), 23300128 (to T.S.) and by MEXT-Supported Program for the Strategic Research Foundation at Private Universities, 2011-2015.

Author Contributions

KSa, TM, TS and YYT designed the research. TM, TK and KSh made the expression vectors and purified the proteins, SK and TF carried out mass spectrometry analysis. KSa and TH performed EM, gold labeling experiments and the analysis. KSa, TM and YYT wrote the manuscript.

Abbreviations List

EM: electron microscopy

CC1: coiled coil 1

CC2: coiled coil 2

HR-region: helix-rich region

SBP: streptavidin-binding peptide

His-tag: octa-histidine tag

References

Akhmanova A, Steinmetz MO (2008) Tracking the ends: a dynamic protein network controls the fate of microtubule tips. *Nat Rev Mol Cell Biol* **9**(4):309-22

Ayloo S, Lazarus JE, Dodda A, Tokito M, Ostap EM, Holzbaur EL. (2014) Dynactin functions as both a dynamic tether and brake during dynein-driven motility. *Nat Commun* **5**:4807.

Baumbach J, Murthy A, McClintock MA, Dix CI, Zalyte R, Hoang HT, Bullock SL (2017) Lissencephaly-1 is a context-dependent regulator of the human dynein complex. *Elife* **6**: e21768.

Cheong FK, Feng L, Sarkeshik A, Yates JR 3rd, Schroer TA (2014) Dynactin integrity depends upon direct binding of dynamitin to Arp1. *Mol Biol Cell* **25**(14): 2171-2180

Culver-Hanlon TL, Lex SA, Stephens AD, Quintyne NJ, King SJ (2006) A microtubule-binding domain in dynactin increases dynein processivity by skating along microtubules. *Nat Cell Biol* **8**(3)**:** 264-270

Dixit R, Levy JR, Tokito M, Ligon LA, Holzbaur EL (2008) Regulation of dynactin through the differential expression of p150Glued isoforms. *J Biol Chem* **283**(48)**:** 33611-33619

Duellberg C, Trokter M, Jha R, Sen I, Steinmetz MO, Surrey T (2014) Reconstitution of a hierarchical +TIP interaction network controlling microtubule end tracking of dynein. *Nat Cell Biol* **16**(8):804-11.

Echeverri CJ, Paschal BM, Vaughan KT, Vallee RB (1996) Molecular characterization of the 50-kD subunit of dynactin reveals function for the complex in chromosome alignment and spindle organization during mitosis. *J Cell Biol* **132**(4)**:** 617-633

Eckley DM, Gill SR, Melkonian KA, Bingham JB, Goodson HV, Heuser JE, Schroer TA (1999) Analysis of dynactin subcomplexes reveals a novel actin-related protein associated with the arp1 minifilament pointed end. *J Cell Biol* **147**(2)**:** 307-320

Fan SS, Ready DF (1997) Glued participates in distinct microtubule-based activities in Drosophila eye development. *Development* **124**(8):1497-507.

Farrer MJ, Hulihan MM, Kachergus JM, Dachsel JC, Stoessl AJ, Grantier LL, Calne S, Calne DB, Lechevalier B, Chapon F, Tsuboi Y, Yamada T, Gutmann L, Elibol B, Bhatia KP, Wider C, Vilarino-Guell C, Ross OA, Brown LA, Castanedes-Casey M, Dickson DW, Wszolek ZK (2009) DCTN1 mutations in Perry syndrome. *Nat Genet* **41**(2)**:** 163-165

Fujimura T, Shinohara Y, Tissot B, Pang PC, Kurogochi M, Saito S, Arai Y, Sadilek M, Murayama K, Dell A, Nishimura S, Hakomori SI (2008) Glycosylation status of haptoglobin in sera of patients with prostate cancer vs. benign prostate disease or normal subjects. *Int J Cancer* **122**: 39–49

Guesdon A, Bazile F, Buey RM, Mohan R, Monier S, García RR, Angevin M, Heichette C, Wieneke R, Tampé R, Duchesne L, Akhmanova A, Steinmetz MO, Chrétien D (2016) EB1 interacts with outwardly curved and straight regions of the microtubule lattice. *Nat Cell Biol* **18**(10):1102-8.

Hayashi T, Saito T, Fujimura T, Hara K, Takamochi K, Mitani K, Mineki R, Kazuno S, Oh S, Ueno T, Suzuki K, Yao T. (2013) Galectin-4, a novel predictor for lymph node metastasis in lung adenocarcinoma. *PLoS One* **8**(12):e81883

Hodgkinson JL, Peters C, Kuznetsov SA, Steffen W (2005) Three-dimensional reconstruction of the dynactin complex by single-particle image analysis. *Proc Natl Acad Sci U S A* **102**(10)**:** 3667-3672

Ichikawa M, Saito K, Yanagisawa HA, Yagi T, Kamiya R, Yamaguchi S, Yajima J, Kushida Y, Nakano K, Numata O, Toyoshima YY (2015) Axonemal dynein light chain-1 locates at the microtubule-binding domain of the γ heavy chain. *Mol*

Biol Cell **26**(23):4236-47.

Ichikawa M, Watanabe Y, Murayama T, Toyoshima YY (2011) Recombinant human cytoplasmic dynein heavy chain 1 and 2: observation of dynein-2 motor activity in vitro. *FEBS Lett* **585**(15)**:** 2419-2423

Imai H, Narita A, Schroer TA, Maeda Y (2006) Two-dimensional averaged images of the dynactin complex revealed by single particle analysis. *J Mol Biol* **359**(4)**:** 833-839

Imai H, Narita A, Maéda Y, Schroer TA (2014) Dynactin 3D structure: implications for assembly and dynein binding. *J Mol Biol* **426**(19): 3262-3271

Ishihara K, Nguyen PA, Groen AC, Field CM, Mitchison TJ (2014) Microtubule nucleation remote from centrosomes may explain how asters span large cells. *Proc Natl Acad Sci USA* **111**(50):17715-22.

Jacquot G, Maidou-Peindara P, Benichou S (2010) Molecular and functional basis for the scaffolding role of the p50/dynamitin subunit of the microtubule-associated dynactin complex. *J Biol Chem* **285**(30)**:** 23019-23031

Jha R, Roostalu J, Cade NI, Trokter M, Surrey T (2017) Combinatorial regulation of the balance between dynein microtubule end accumulation and initiation of directed motility. *EMBO J* **36**(22):3387-3404.

Kardon JR, Reck-Peterson SL, Vale RD (2009) Regulation of the processivity and intracellular localization of Saccharomyces cerevisiae dynein by dynactin. *Proc Natl Acad Sci U S A* **106**(14)**:** 5669-5674

Kardon JR, Vale RD (2009) Regulators of the cytoplasmic dynein motor. *Nat Rev Mol Cell Biol* **10**(12)**:** 854-865

Karki S, Holzbaur EL (1995) Affinity chromatography demonstrates a direct binding between cytoplasmic dynein and the dynactin complex. *J Biol Chem* **270**(48)**:** 28806-28811

King SJ, Schroer TA (2000) Dynactin increases the processivity of the cytoplasmic dynein motor. *Nat Cell Biol* **2**(1):20-4.

King SJ, Brown CL, Maier KC, Quintyne NJ, Schroer TA (2003) Analysis of the dynein-dynactin interaction in vitro and in vivo. *Mol Biol Cell* **14**(12)**:** 5089-5097

Kitai T, Watanabe Y, Toyoshima YY, Kobayashi T, Murayama T, Sakaue H, Suzuki H, Takahagi T (2011) Simple Method of Synthesizing Nickel–Nitrilotriacetic Acid Gold Nanoparticles with a Narrow Size Distribution for Protein Labeling. *Japanese Journal of Applied Physics* **50:** 095002-095005
http://dx.doi.org/10.1143/JJAP.50.095002

Kobayashi T, Shiroguchi K, Edamatsu M, Toyoshima YY (2006) Microtubule-binding properties of dynactin p150 expedient for dynein motility. *Biochem Biophys Res Commun* **340**(1)**:** 23-28

Kobayashi T, Morone N, Kashiyama T, Oyamada H, Kurebayashi N, Murayama T (2008) Engineering a novel multifunctional green fluorescent protein tag for a wide variety of protein research. *PLoS One* **3**(12):e3822.

Kobayashi T, Murayama T (2009) Cell cycle-dependent microtubule-based dynamic transport of cytoplasmic dynein in mammalian cells. *PLoS One* **4**(11)**:** e7827

Kobayashi T, Miyashita T, Murayama T, Toyoshima YY (2017) Dynactin has two antagonistic regulatory domains and exerts opposing effects on dynein motility. *PLoS One* **12**(8):e0183672

Lloyd TE, Machamer J, O'Hara K, Kim JH, Collins SE, Wong MY, Sahin B, Imlach W, Yang Y, Levitan ES, McCabe BD, Kolodkin AL (2012) The p150(Glued) CAP-Gly domain regulates initiation of retrograde transport at synaptic termini. *Neuron* **74**(2):344-60

Maier KC, Godfrey JE, Echeverri CJ, Cheong FK, Schroer TA (2008) Dynamitin mutagenesis reveals protein-protein interactions important for dynactin structure. *Traffic* **9**(4)**:** 481-491

Mcgrail M, Gepner J, Silvanovich A, Ludmann S, Serr M, Hays TS (1995) Regulation of Cytoplasmic Dynein Function In Vivo by the Drosophila Glued complex. *J. Cell Biol.* **131**(2)**:** 411–425

McGuffin LJ, Bryson K, Jones DT (2000) The PSIPRED protein structure prediction server. *Bioinformatics* **16**(4)**:** 404-405

McKenney RJ, Huynh W, Vale RD, Sirajuddin M (2016) Tyrosination of α-tubulin controls the initiation of processive dynein-dynactin motility. *EMBO J* **35**(11):1175-85

Melkonian KA, Maier KC, Godfrey JE, Rodgers M, Schroer TA (2007) Mechanism of dynamitin-mediated disruption of dynactin. *J Biol Chem* **282**(27)**:** 19355-19364

Miura M, Matsubara A, Kobayashi T, Edamatsu M, Toyoshima YY (2010) Nucleotide-dependent behavior of single molecules of cytoplasmic dynein on microtubules in vitro. *FEBS Lett* **584**(11)**:** 2351-2355

Morgan JL, Song Y, Barbar E (2011) Structural dynamics and multiregion interactions in dynein-dynactin recognition. *J Biol Chem* **286**(45)**:** 39349-39359
Moughamian AJ, Holzbaur EL (2012) Dynactin is required for transport initiation from the distal axon. *Neuron* **74**(2):331-43

Puls I, Jonnakuty C, LaMonte BH, Holzbaur EL, Tokito M, Mann E, Floeter MK, Bidus K, Drayna D, Oh SJ, Brown RH, Jr., Ludlow CL, Fischbeck KH (2003) Mutant dynactin in motor neuron disease *Nat Genet* **33**(4)**:** 455-456

Schafer DA, Gill SR, Cooper JA, Heuser JE, Schroer TA (1994) Ultrastructural analysis of the dynactin complex: an actin-related protein is a component of a filament that resembles F-actin. *J Cell Biol* **126**(2)**:** 403-412

Schroer TA (2004) Dynactin. *Annu Rev Cell Dev Biol* **20:** 759-779

Siglin AE, Sun S, Moore JK, Tan S, Poenie M, Lear JD, Polenova T, Cooper JA, Williams JC (2013) Dynein and dynactin leverage their bivalent character to form a high-affinity interaction. *PLoS One* **8**(4): e59453

Song K, Awata J, Tritschler D, Bower R, Witman GB, Porter ME, Nicastro D (2015) In situ localization of N and C termini of subunits of the flagellar nexin-dynein regulatory complex (N-DRC) using SNAP tag and cryo-electron tomography. *J Biol Chem* **290**(9):5341-53.

Steinmetz MO, Akhmanova A (2008) Capturing protein tails by CAP-Gly domains. *Trends Biochem Sci* **33**(11)**:** 535-545

Suzuki K, Miyazaki M, Takagi J, Itabashi T, Ishiwata S (2017) Spatial confinement of active microtubule networks induces large-scale rotational cytoplasmic flow. *Proc Natl Acad Sci USA* **114**(11):2922-2927.

Swaroop A, Paco-Larson ML, Garen A (1985) Molecular genetics of a transposon-induced dominant mutation in the Drosophila locus Glued. *Proc Natl Acad Sci USA* **82**(6):1751-5.

Tokito MK, Howland DS, Lee VM, Holzbaur EL (1996) Functionally distinct isoforms of dynactin are expressed in human neurons. *Mol Biol Cell* **7**(8)**:** 1167-1180

Tripathy SK, Weil SJ, Chen C, Anand P, Vallee RB, Gross SP (2014) Autoregulatory mechanism for dynactin control of processive and diffusive dynein transport. *Nat Cell Biol.* **16**(12):1192-1201

Urnavicius L, Zhang K, Diamant AG, Motz C, Schlager MA, Yu M, Patel NA, Robinson CV, Carter AP. (2015) The structure of the dynactin complex and its interaction with dynein. *Science* **347**(6229):1441-1446

Vaughan KT, Vallee RB (1995) Cytoplasmic dynein binds dynactin through a direct interaction between the intermediate chains and p150Glued. *J Cell Biol* **131**(6 Pt 1)**:** 1507-1516

Wang Q, Crevenna AH, Kunze I, Mizuno N (2014) Structural basis for the extended CAP-Gly domains of p150(glued) binding to microtubules and the implication for tubulin dynamics. *Proc Natl Acad Sci U S A* **111**(31):11347-52

Waterman-Storer CM, Karki S, Holzbaur EL (1995) The p150Glued component of the dynactin complex binds to both microtubules and the actin-related protein centractin (Arp-1). *Proc Natl Acad Sci U S A* **92**(5)**:** 1634-1638

Weisbrich A, Honnappa S, Jaussi R, Okhrimenko O, Frey D, Jelesarov I, Akhmanova A, Steinmetz MO (2007) Structure-function relationship of CAP-Gly domains. *Nat Struct Mol Biol* **14**(10)**:** 959-967

Yeh TY, Quintyne NJ, Scipioni BR, Eckley DM, Schroer TA (2012) Dynactin's pointed-end complex is a cargo-targeting module. *Mol Biol Cell* **23**(19)**:** 3827-3837

Yeh TY, Kowalska AK, Scipioni BR, Cheong FK, Zheng M, Derewenda U, Derewenda ZS, Schroer TA (2013) Dynactin helps target Polo-like kinase 1 to kinetochores via its left-handed beta-helical p27 subunit. *EMBO J* **32**(7)**:** 1023-1035

Zhapparova ON, Bryantseva SA, Dergunova LV, Raevskaya NM, Burakov AV, Bantysh OB, Shanina NA, Nadezhdina ES (2009) Dynactin subunit p150Glued isoforms notable for differential interaction with microtubules. *Traffic* **10**(11)**:** 1635-1646

Saito et al. –Fig. 1

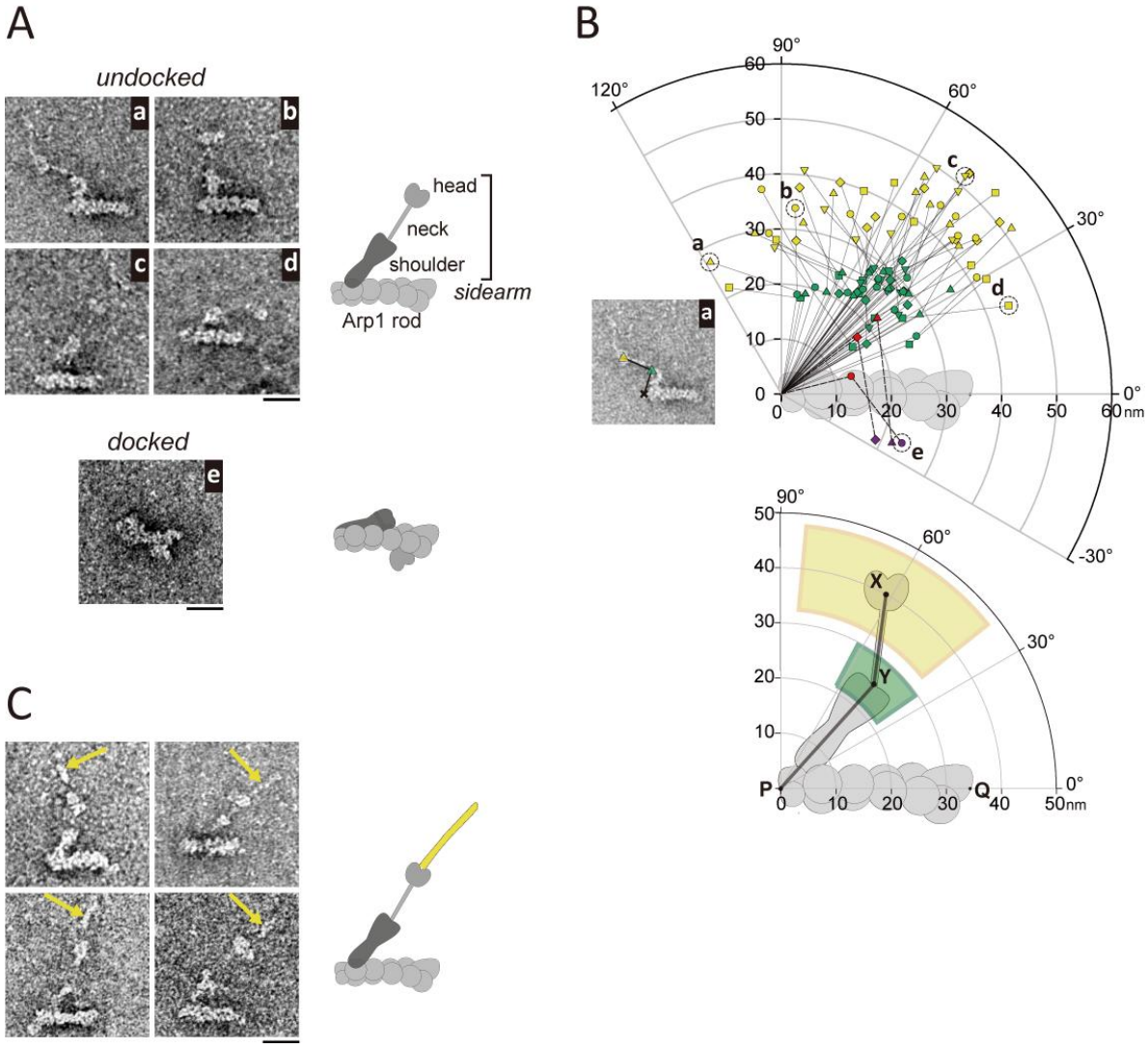

Figure 1. Negative stain EM of the human dynactin complex revealed morphological diversity of the sidearm and a thin filamentous structure at the tip. (A) Left, negative stain EM images of the dynactin complexes (SBP-p62). Each molecule exhibits the distinguishable Arp1 rod, shoulder, neck and head domains, except the molecule in the lower panel (e) in which the Arp1 rod is overlapped with the neck and the part of the shoulder. The gallery shows the diverse morphologies of the sidearm, including the undocked sidearm (a-d) and the docked sidearm (e). Right, cartoons to illustrate the morphological features and the configurations of the dynactin complexes. (B) Quantitative comparison of the geometry of the sidearms. Upper, the polar coordinates of the head and the neck-shoulder junction (base of neck) are shown. For the undocked sidearm, the yellow and the green plots indicates the positions of the head and base of the neck, respectively. For the docked sidearm, the purple and red plots indicate the positions of the head and base of the neck, respectively. For each molecule, the head and base of the neck are determined as illustrated in **Fig. S3A, middle,** and those positions are measured and mapped by setting the origin at the barbed end, to compare the orientation of the sidearm among molecules. See also **Fig. S3A** and **Materials and methods** for details. The data set is composed of dynactin molecules (SBP-p62) in which the reference points described above are clearly observed, with the undocked sidearm (yellow and green, $N = 48$) and the docked sidearm (purple and red, $N = 3$). Each polygonal line connecting the origin and the two plotted points indicates the backbone of the sidearm of each molecule (corresponding to the polygonal line X-Y-P in the right graph). To help distinguish between molecules, the sets of yellow and green (or red and purple) plots are marked with several symbols (circle, triangle up, triangle down, square, diamond). The plots labeled (a) to (e) represents the molecules shown in **(A)**, and the molecule (a) are shown here again as an example of the measurement. Lower, the

graph represents the mean and SD values of the head (yellow) and the base of neck (yellow) in the undocked form of the sidearm. The values are 40.0 ± 7.6 nm and 61.4 ± 23.1° for the head (X) (N= 48) and 25.4 ± 4.3 nm and 47.9 ±13.5° for the base of neck (Y) (N= 48). (C) Left, thin filamentous structures (yellow arrows) adjoining the head domain were observed in some molecules. Right, a cartoon to illustrate the dynactin complex with the filamentous structure (yellow). Bars represent 20 nm.

Saito et al. –Fig. 2

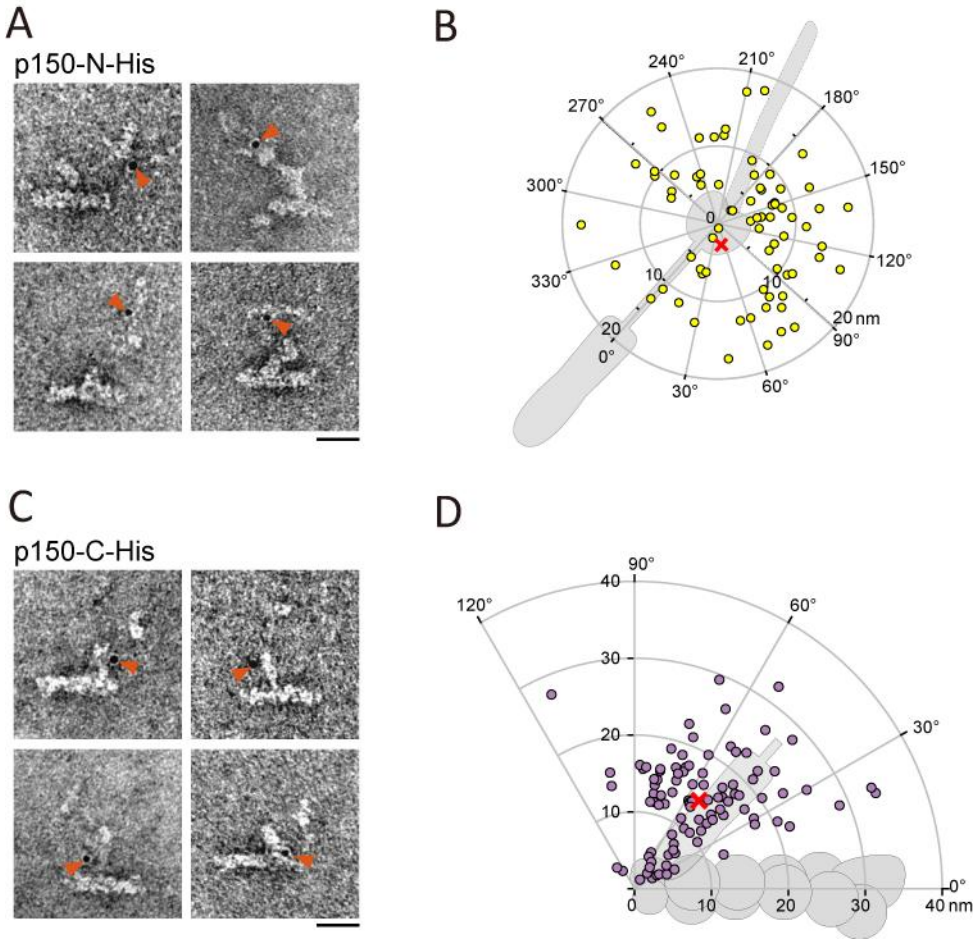

Figure 2. Localization of the N- and C- termini of p150 within the dynactin complex. (A) EM images of a mutant complex (p150-N-His) labeled with Ni-NTA gold nanoparticles (red arrowheads). (B) Distribution of the gold nanoparticles bound to p150-N-His. The polar coordinates of the centroid (red cross) are (2.8 nm, 51°) (N= 74). (C) EM images of a mutant complex (p150-C-His) labeled with the gold nanoparticles (red arrowheads). (D) The distribution of the gold nanoparticles bound to p150-C-His. The polar coordinates of the centroid (red cross) are (14.2 nm, 54°) (N= 98). Bars represent 20 nm.

Saito et al. –Fig. 3

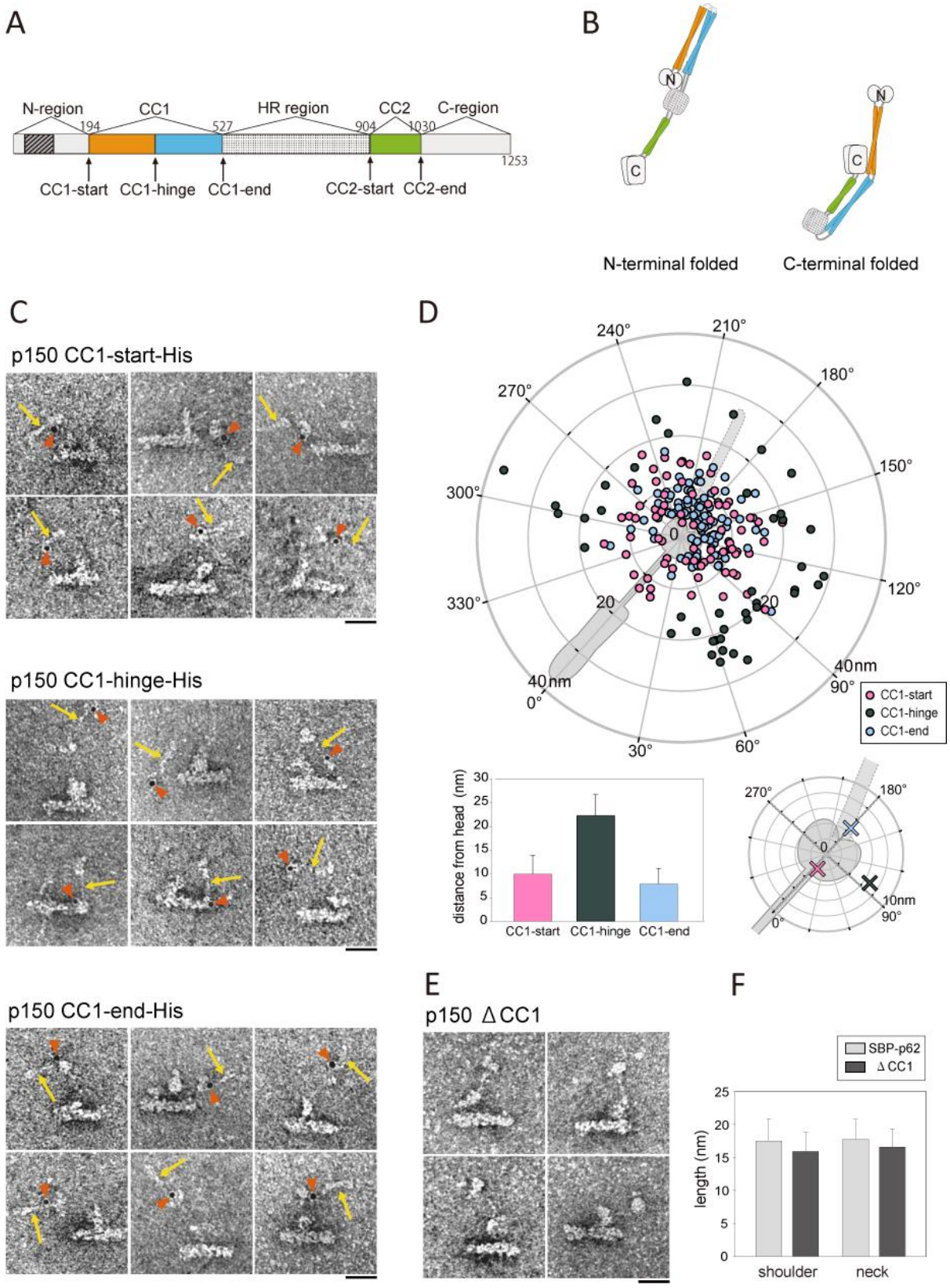

Figure 3. Identification of the p150 CC1 region. (A) Diagram of the p150 sequence divided into five regions: N-, CC1, HR (helix-rich), CC2 and C-regions. The CAP-Gly domain (hatched), CC1a (orange), CC1b (light blue) and CC2 (light green) are indicated. (B) Two possible folding patterns of p150. Left, CC1 folds back at the hinge and CC2 forms the neck domain (N-terminal folded model). Right, CC1 forms the neck domain and folds back at the region between CC1b and CC2 (C-terminal folded model). (C) EM images of the nanogold-labeled mutants, p150 CC1-start-His (top), p150 CC1-hinge-His (middle) and p150 CC1-end-His (bottom). Red arrowheads indicate the gold nanoparticles and yellow arrows indicate the thin filamentous structure. (D) Upper, the distribution of the gold nanoparticles bound to p150 CC1-start-His (pink) (N= 76), p150 CC1-hinge-His (dark green) (N= 41) and p150 CC1-end-His (light blue) (N= 110). Lower left, the distance between the gold nanoparticles and the center of the heads. Lower right, the polar coordinates of the centroid are (2.2 nm, 12°), (6.8 nm, 99°) and (4.6 nm, 179°) for p150 CC1-start-His (pink) (N = 76), p150 CC1-hinge-His (dark green) (N = 41) and p150 CC1-end-His (light blue) (N = 110), respectively. (E) Negative stain EM images of the CC1 deleted p150 (p150 ΔCC1) dynactin complex. (F) Comparison of the lengths of the shoulder and the neck between p150 ΔCC1 and the wild type p150 (SBP-p62). The lengths of the shoulder (the segment YZ in **Fig. S4B**) of SBP-p62 and p150 ΔCC1 were 17.5 ± 3.3 nm (N= 50) and 15.9 ± 2.9 nm (N= 40), respectively (mean ± SD). The lengths of the neck (the segment XY in **Fig. S4B**) of SBP-p62 and p150 ΔCC1 were 17.7 ± 3.0 nm (N= 50) and 16.6 ± 2.8 nm (N= 40), respectively (mean ± SD) (Welch's t-test, p = 0.02 for the shoulder and 0.06 for the neck). Bars represent 20 nm.

Saito et al. –Fig. 4

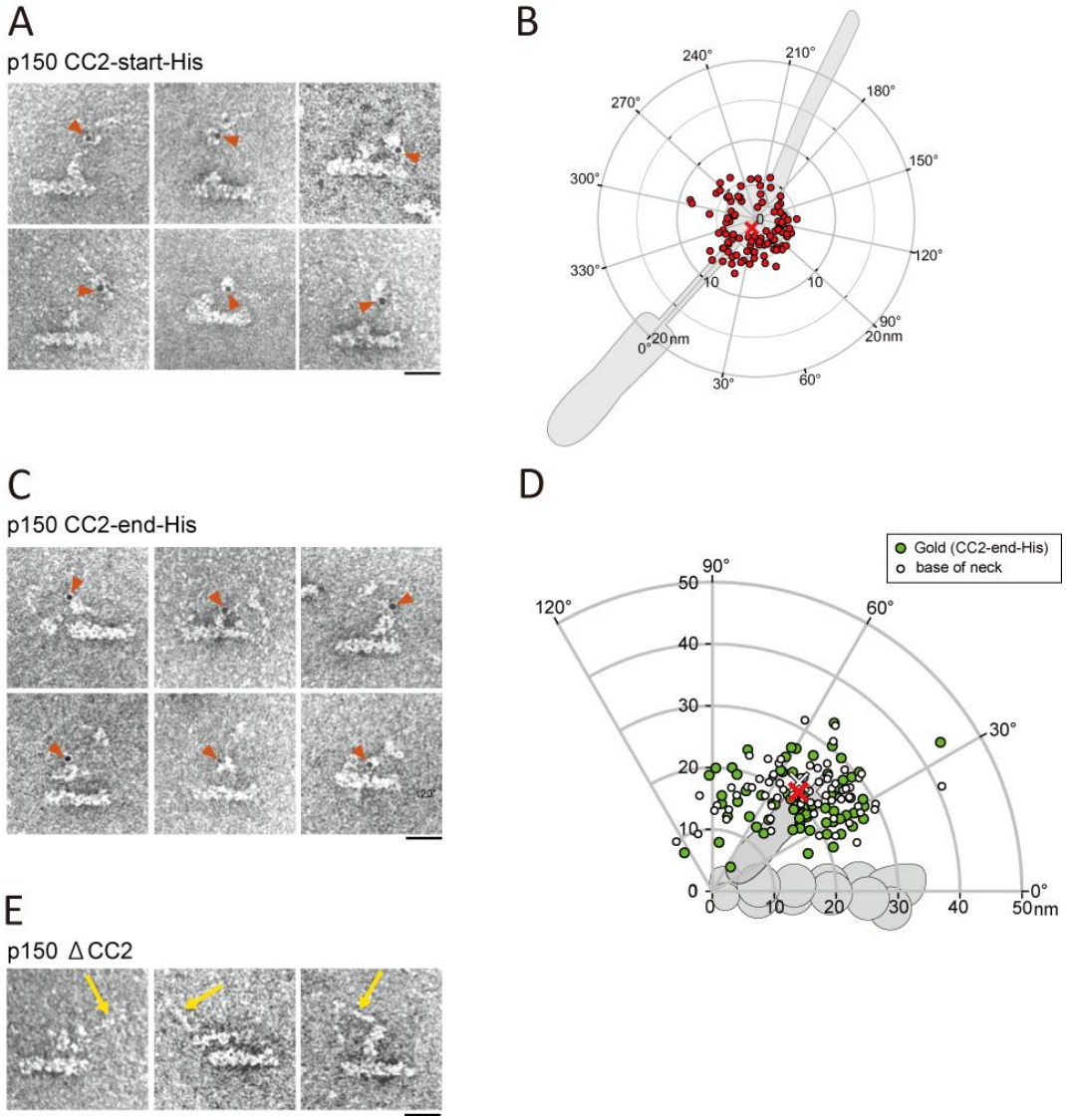

Figure 4. Identification of the p150 CC2 region. (A) EM images of p150 CC2-start-His labeled with the gold nanoparticles (red arrowheads). (B) The distribution of the gold nanoparticles bound to p150 CC2-start-His. The polar coordinates of the centroid (red cross) were (1.2 nm, 15°) (N = 95). (C) EM images of p150 CC2-end-His labeled with the gold nanoparticles (red arrowheads). (D) The distribution of the gold nanoparticles in the p150 CC2-end-His mutant (green circles) (N = 73). For comparison, the position of base of the neck (point Y in **Fig. S3A**) is shown for the same data set (white triangles). The red cross indicates the centroid of the gold nanoparticles (20.3 nm, 46°) and the white cross indicates the centroid of the base of neck (21.5 nm, 48°). (E) EM images of p150 ΔCC2. Yellow arrows indicate the protrusion formed by CC1. Bars represent 20nm.

Saito et al. –Fig. 5

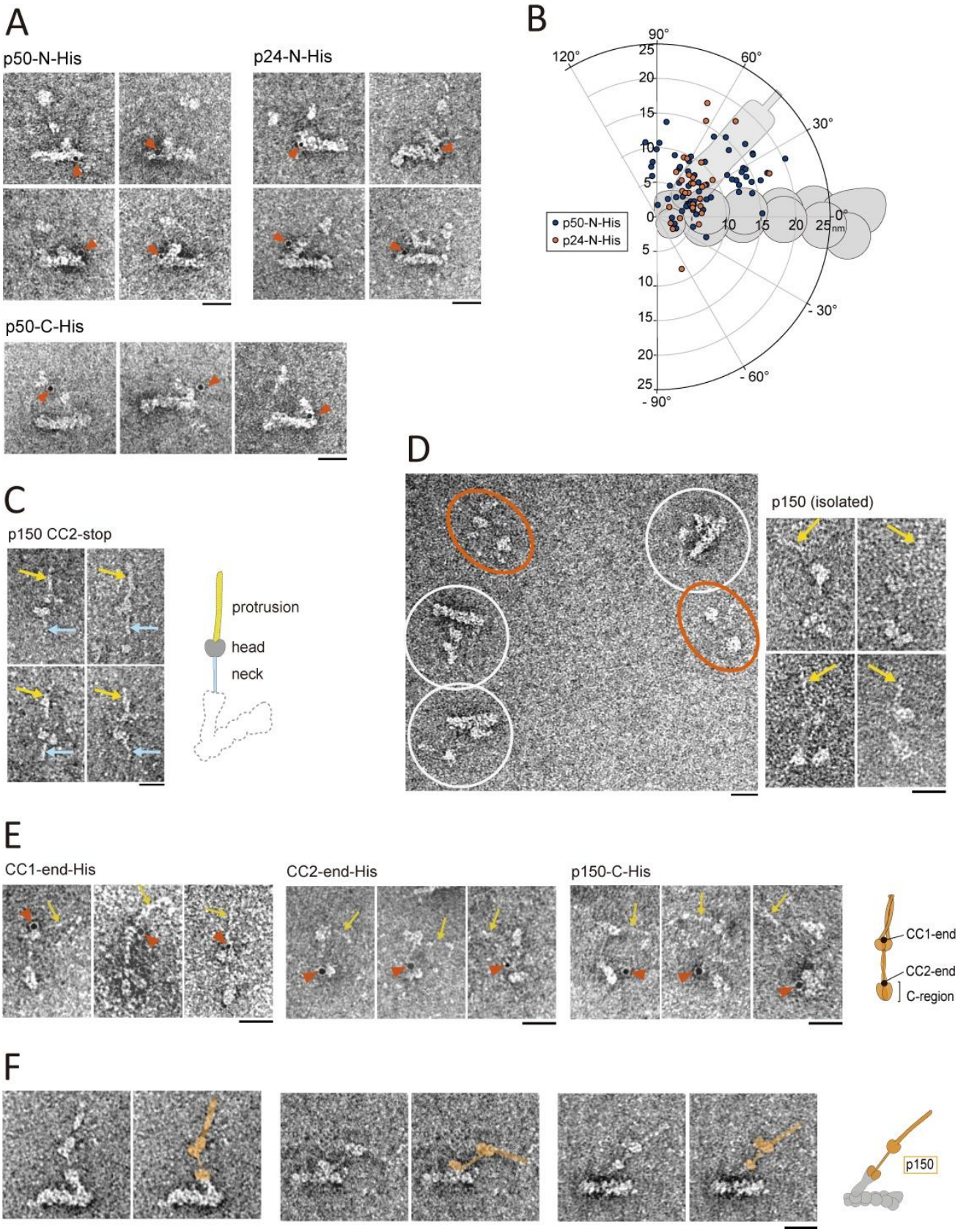

Figure 5. The shoulder domain is formed by p50, p24 and C-region of p150. (A) EM images of p50-N-His (upper left), p24-N-His (upper right) and p50-C-His (lower) labeled with the gold nanoparticles (red arrowheads). See also **Fig. S5A**. (B) The distribution of the gold nanoparticles in p50-N-His (dark blue, $N = 64$) and in p24-N-His (orange, $N = 32$). (C) EM images of p150 CC2-stop, which lacks the C-region. The head, the protrusion formed by CC1 (yellow arrows) and the neck formed by CC2 (light blue arrows) are observed but the shoulder and the Arp1 rod are not, as illustrated in the cartoon on the right. (D) Left, a general view of the EM image of a mutant complex (p150-N-His). As well as the dynactin complex (white circles), isolated p150 particles (orange ellipses) are seen because the mutant p150 is more abundant than other subunits in cells exogenously expressing p150. Right, a gallery of EM images of isolated p150 dimers (p150-N-His) (E) EM images of isolated p150 dimers that are not incorporated into the dynactin complex in the mutants of p150: p150 CC1-end-His (left), p150 CC2-end-His (middle), p150-C-His (right). Gold nanoparticles (red arrowheads) are bound to their His-tagged sites and the CC1 protrusion (yellow arrows) are observed. (F) Pairs of EM images of the dynactin complex (SBP-p62, containing a wild type sidearm) and identical ones with the supposed location of p150 pseudo-colored in orange. Bars represent 20 nm.

Saito et al. –Fig. 6

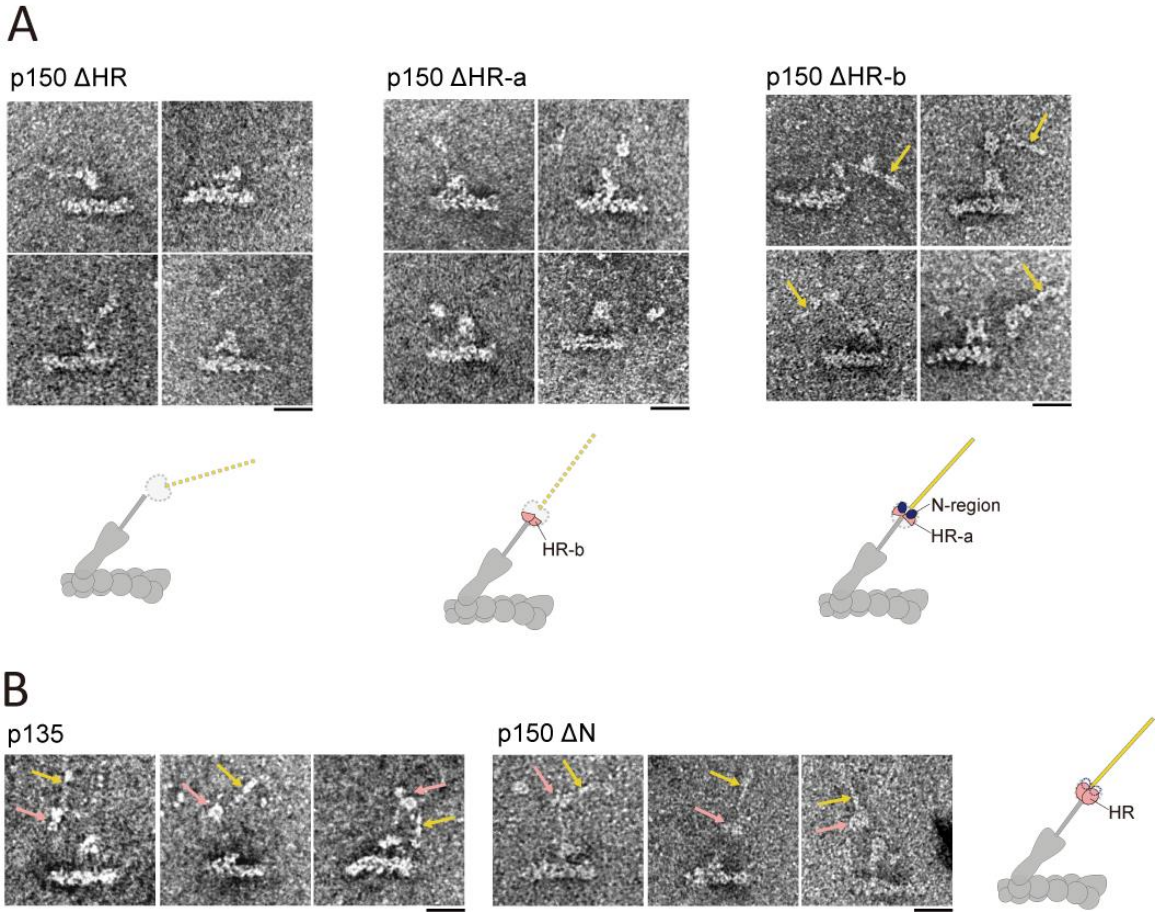

Figure 6. Identification of the p150 HR region. (A) EM images of p150 ΔHR (left), p150 ΔHR-a (middle) and p150 ΔHR-b (right). Yellow arrows indicate the CC1 protrusions. (B) EM images of the p150 mutants lacking the N-region: p135 (left) and p150 ΔN (right). Yellow arrows indicate the CC1 protrusions. Pink arrows indicate the head domain formed by the HR region without the N-region.

Saito et al. –Fig. 7

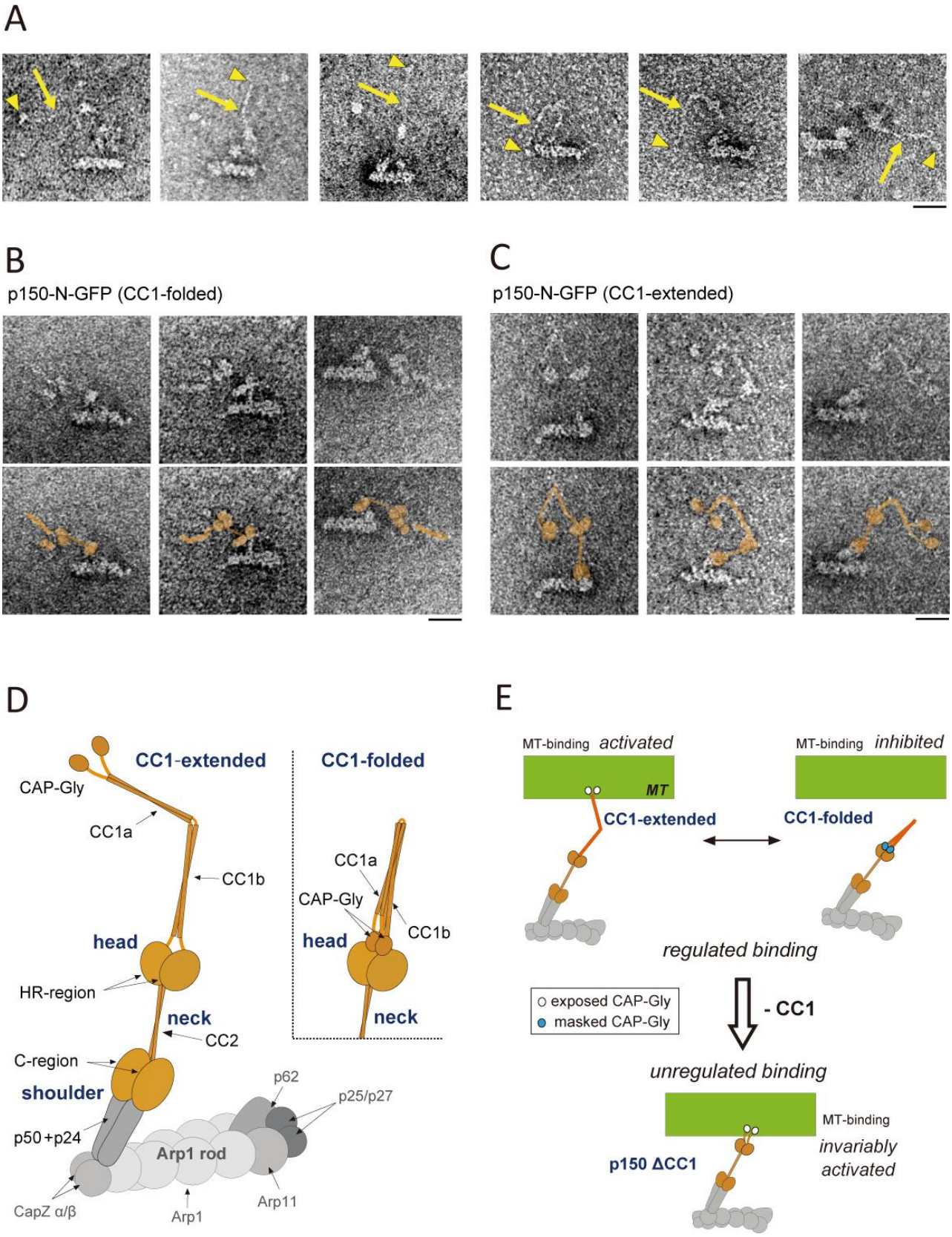

Figure 7. Conformational change of CC1 and new model of the dynactin sidearm. (A) EM images of a subset of SBP-p62 with longer CC1 protrusion (yellow arrows). Yellow arrowheads indicate N-region, the tip of the CC1 protrusion. (B), (C) Pairs of EM images of p150-N-GFP and identical ones with the supposed location of p150 pseudo-colored in orange. (B) The HR region and the GFP + N-region are in proximity at the bottom of the CC1 protrusion (CC1-folded). (C) The HR region and the GFP + N-region are observed as separate and distinguishable structures, with these two domains bridged by a hooked CC1 (CC1-extended). Bars represent 20 nm. (D) New model of the dynactin sidearm. The sidearm is composed of four domains: a CC1 protrusion, two heads, a neck and a shoulder. p150 is colored orange and each domain in p150 is indicated. The CC1 protrusion takes a folded form (upper) and an extended form (lower). The model of the Arp1 rod and the composition of the shoulder are based on the previous reports (Eckley et al., 1999; Imai et al., 2006; Maier et al., 2008; Schroer, 2004; Urnavicius et al., 2015). (E) A proposed model for the regulation of MT-binding through the conformational change of the CC1-arm. When the CC1-arm takes the extended form, CAP-Gly is exposed and MT-binding is activated (upper left), whereas when the CC1-arm takes the folded form, CAP-Gly is masked and MT-binding is inhibited (upper right). Deletion of the CC1 domain impairs this regulation and the p150 ΔCC1 mutant exhibits unregulated stable binding to MTs (lower).

Saito et al. –Fig. S1

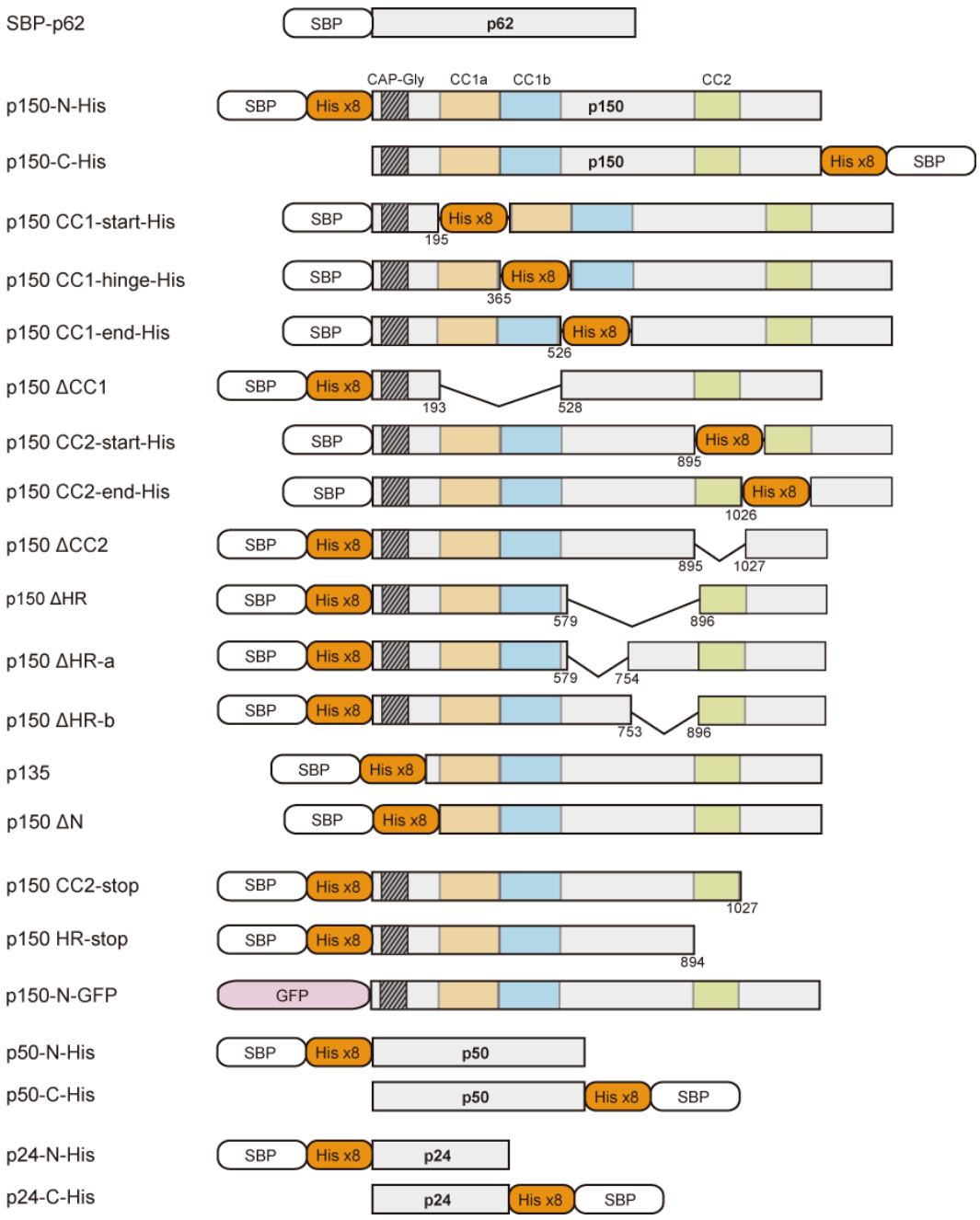

Figure S1. Constructs used in this study. The octa-histidine tag (His-tag) flanked by short linkers (GGGSHHHHHHHHGGGS) was inserted after K195, K365, Q526, E895, and E1026 for CC1-start-His, CC1-hinge-His, CC1-end-His, CC2-start-His, and CC2-end-His, respectively. For the other mutants, the His-tag was fused at either the N- or C-terminus. The residues S194-Q527, R896-E1026, G580-E895, G580-G753, and G754-E895 were deleted in ΔCC1, ΔCC2, ΔHR, ΔHR-a, and ΔHR-b, respectively. A C-terminal region encompassing E895-S1253 and L1028-S1253 was truncated in CC2-stop and HR-stop, respectively. Note that a His-tag and a SBP-tag were included in the GFP of the p150-N-GFP construct (see **Materials and methods**).

Saito et al. –Fig. S2

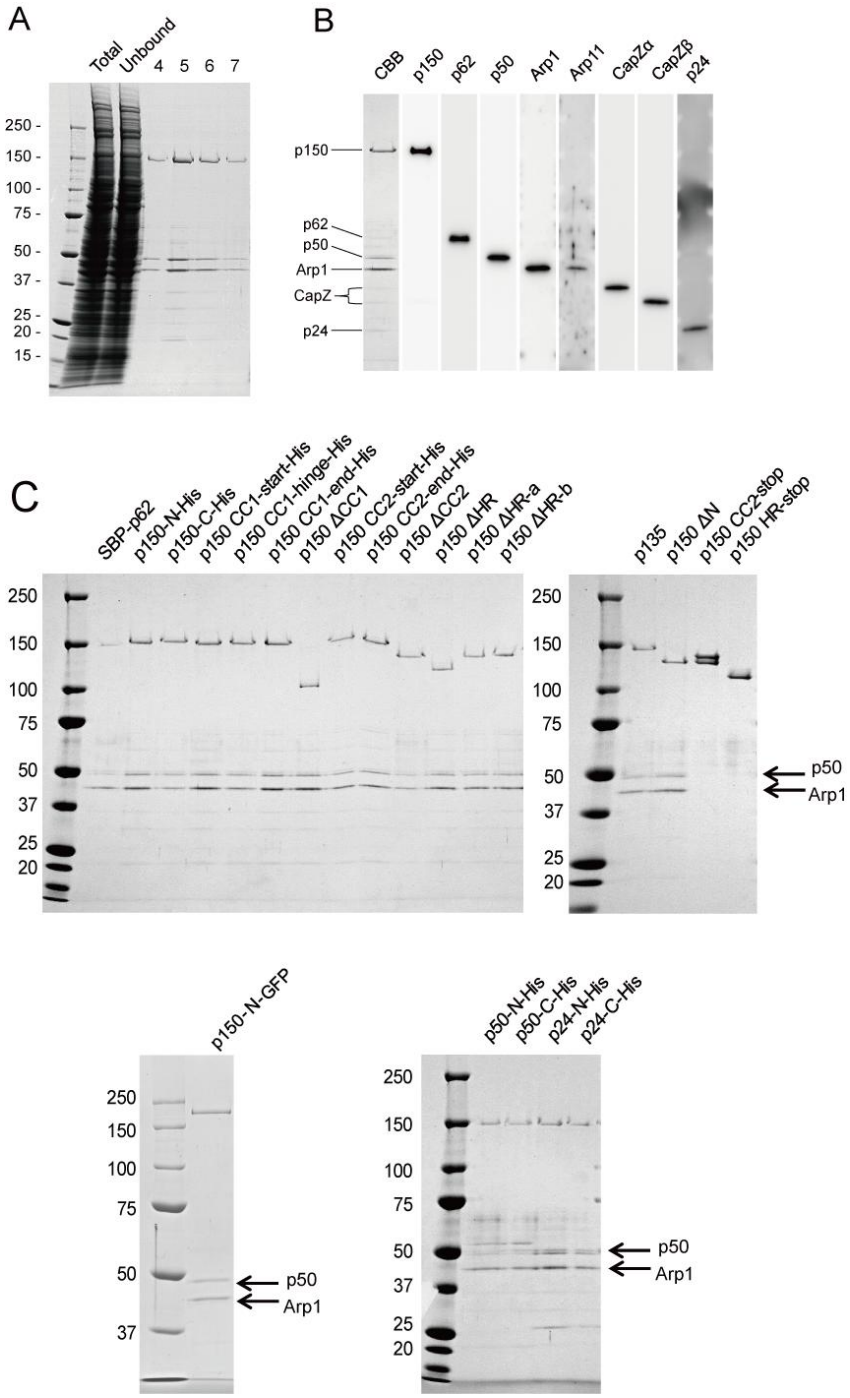

Figure S2. Sample preparation of recombinant human dynactin. (A) Purification of the dynactin complex by StrepTrap column chromatography. SDS-polyacrylamide gel (3%–15%) of the lysate from HEK-293 cells expressing p150-N-His (Total), the unbound fraction from the column (Unbound), and the eluted fractions No. 4–7. (B) Western blotting of the purified p150-N-His (No. 5 fraction in (A)). The purified fraction contained all the dynactin subunits examined (p150, p62, p50, Arp1, Arp11, CapZα, CapZβ, and p24). (C) SDS-polyacrylamide gels of the purified dynactin mutants used in this study. p50 and Arp1 bands (arrows) were clearly detected in all the mutants except for p150 CC2-stop and p150 HR-stop. Lower bands in p150 CC2-stop may be a degradation product.

Saito et al. –Fig. S3

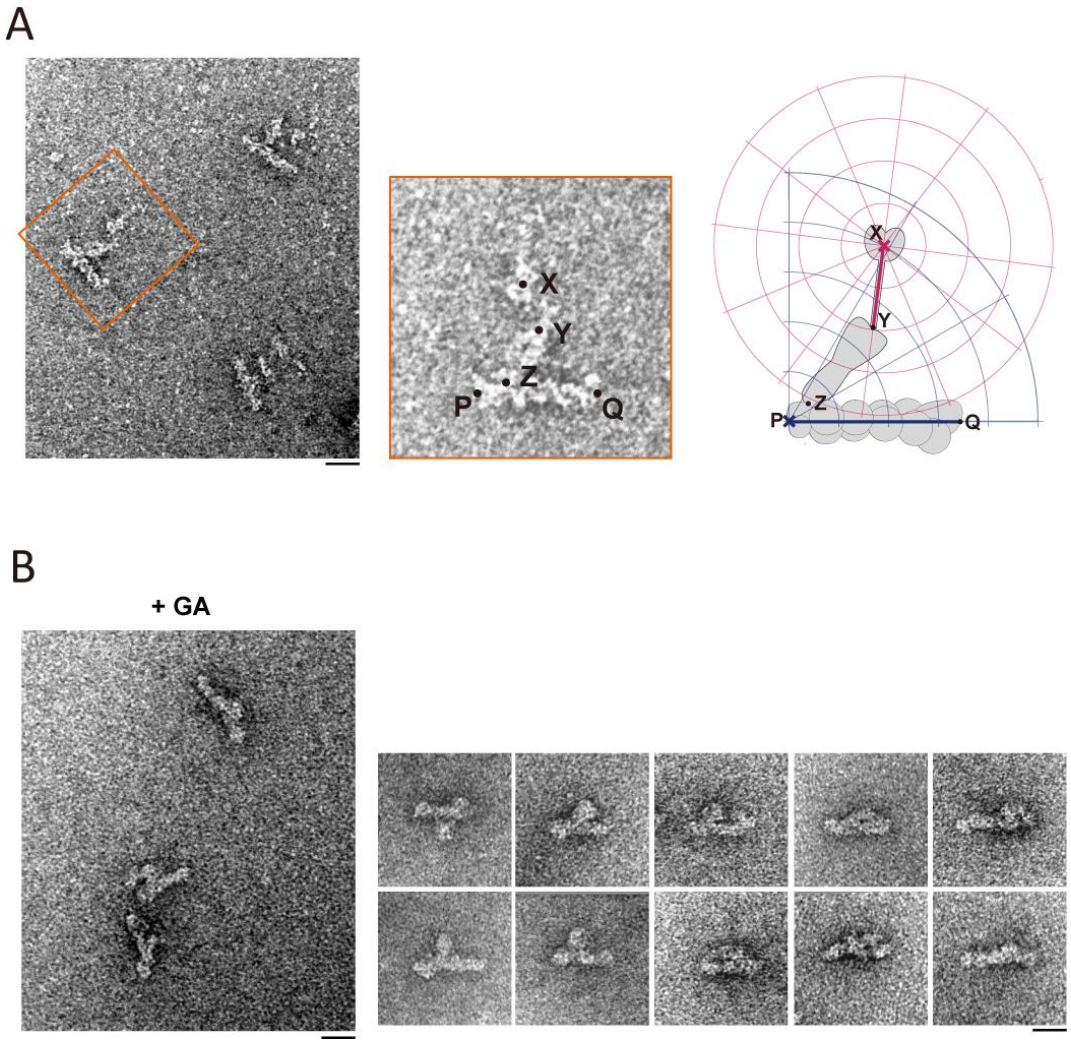

Figure S3. Morphological features of the dynactin complex and the effect of glutaraldehyde fixation. (A) Morphological features of the dynactin complex. Left, a general view of the negative stain EM image of the dynactin complex (SBP-p62). Middle, a magnified image of the molecule designated by the orange box in the left general view. Points are assigned to show the morphological features of the dynactin complex and to define the reference points in it. P: barbed end of the Arp1 rod; Q: pointed end of the Arp1 rod; X: center of the two heads; Y: the neck-shoulder junction (base of neck); Z: proximal end of the shoulder. Right, illustration of coordinate system settings used in the measurement of dynactin complex or nanogold labeling. See **Materials and methods** for details. (B) Glutaraldehyde fixation of the dynactin complex. Left, a general view; right, a gallery of molecules with the docked sidearm. The dynactin complex (SBP-p62), which includes wild type p150, was fixed with 2 % glutaraldehyde for 30 min on ice and then negatively stained. In most molecules, the shoulder appeared to closely contact with the Arp1 rod, and the neck, the head and the CC1-arm were not able to be recognized as distnguishable structures. Lower concentrations of glutaraldehyde(0.5 %, 1 %) and shorter periods of fixation time (5 min, 10 min) did not alter the result. Bars represent 20 nm.

Saito et al. –Fig. S4

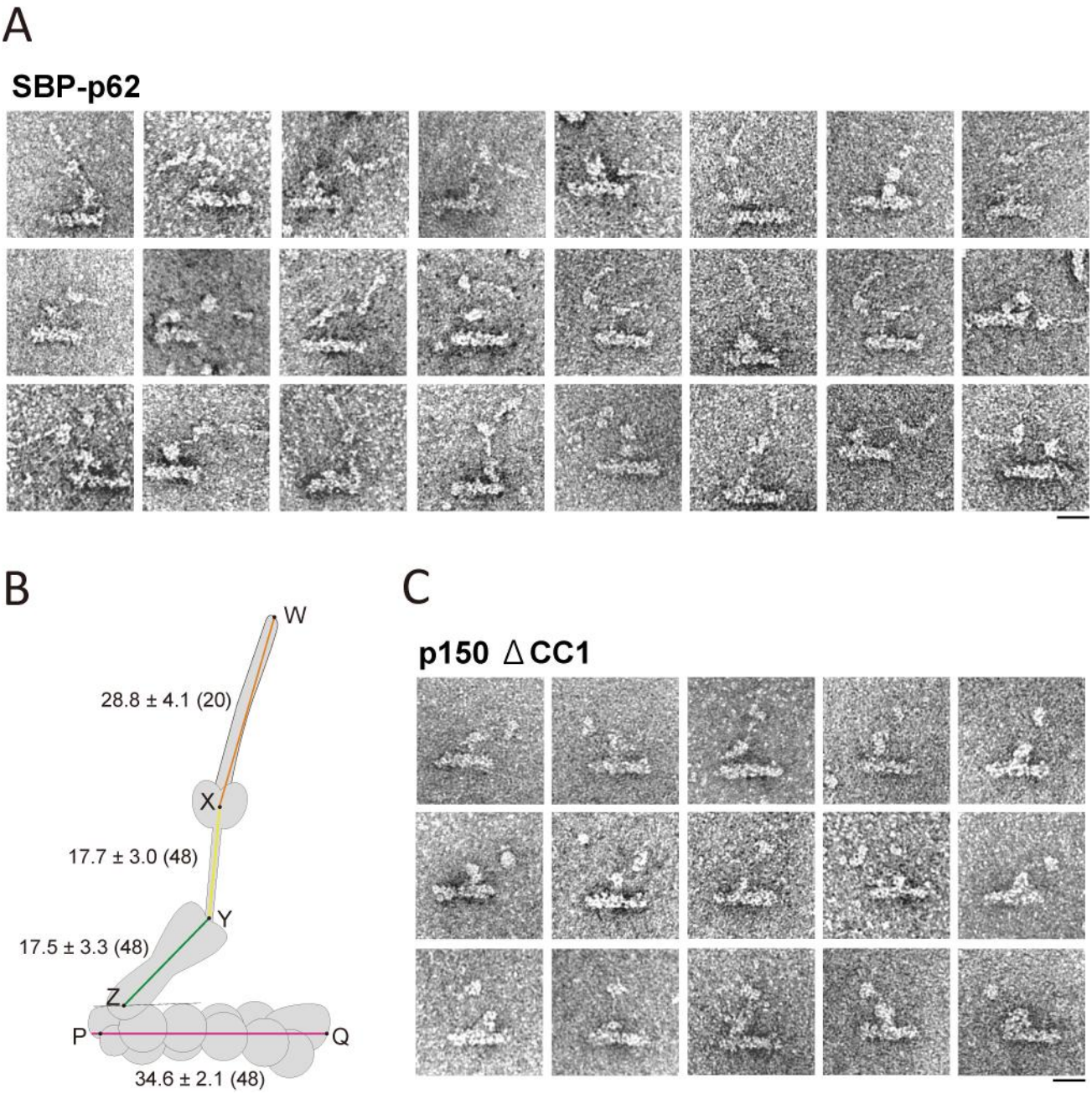

Figure S4. Comparison of the wild type p150 and p150 ΔCC1. (A) A gallery of EM images of SBP-p62 containing a wild-type sidearm. Molecules with the filamentous structure were selected here (corresponding to **Fig. 1C**). (B) The average lengths (mean ± SD (*N*)) (nm) between the reference points. The definition of the reference points are the same as **Fig. S3A**, except for the tip of the filament (W). The data set is the same as the dynactin molecules with the undocked form in **Fig. 1B** ($N = 48$). The data set includes a subset of molecules in which the tip of the filament was specified ($N = 20$). (C) A gallery of EM images of p150 ΔCC1 containing a CC1-deleted sidearm.

Saito et al. –Fig. S5

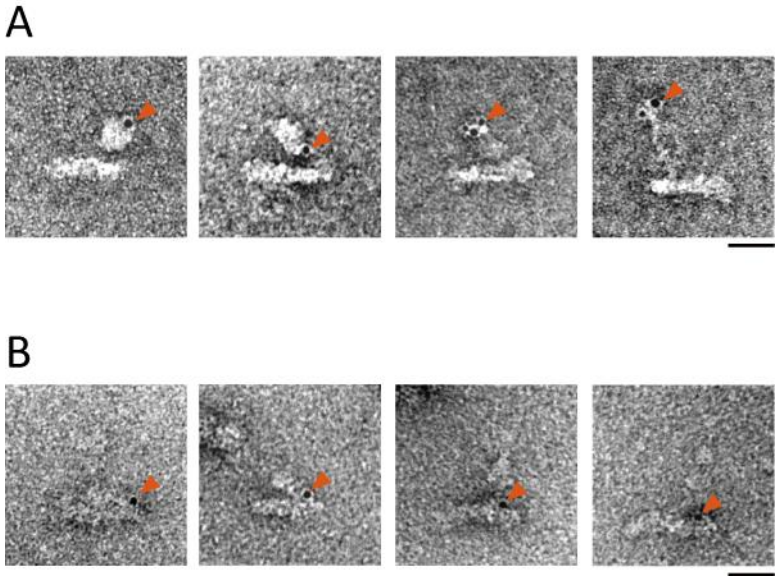

Figure S5. EM images and gold labeling of p50-C-His and p24-C-His mutants. (A) The dynactin complex of p50-C-His showing an irregular form of the sidearm. The sidearm in this mutant exhibited bigger and more expanded appearance than those of other mutants, in which the components of the sidearm might be misfolded (left two panels). In another case, a thin structure, which might be an unfolded form of p50, was observed to extend from the Arp1 rod (rightmost panel). Bound gold particles (red arrowheads) show the site of the C-terminus of p50 in each molecule. (B) The dynactin complex of the p24 mutant to which SBP and His tags are added to the C terminus of p24 in this order. Thus, the gold particles indicate the position of the SBP C-terminus. Bars represent 20 nm.

Saito et al. –Fig. S6

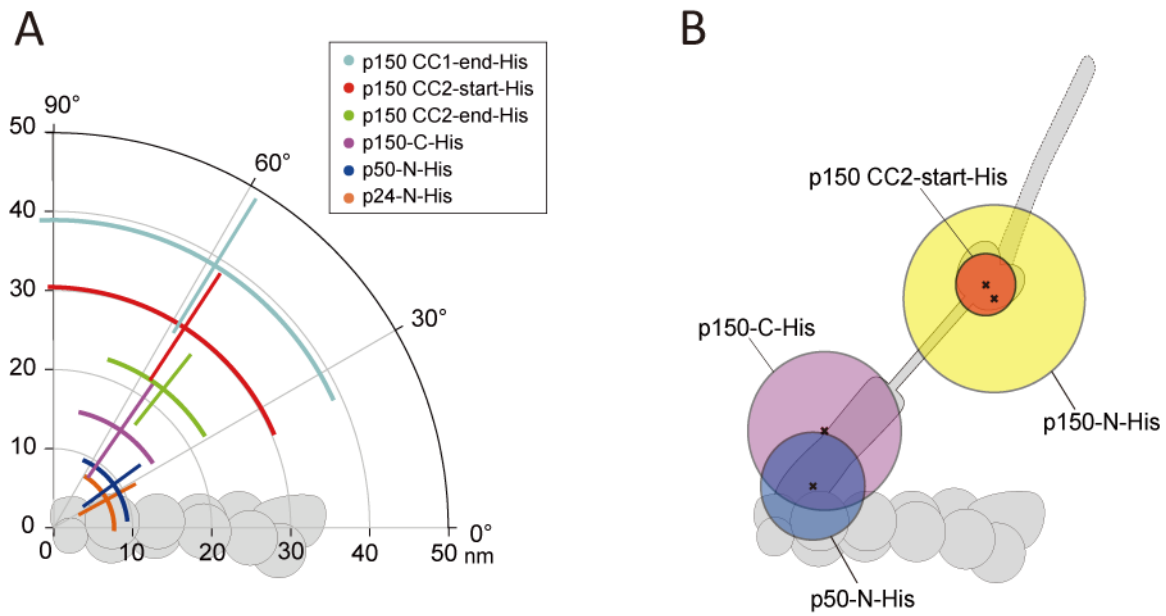

Figure S6. Distribution maps of the nanogold-labeled sites in the sidearm. (A) Summary of the nanogold labeling of representative mutants. Here, the positions of the gold nanoparticles were measured from the barbed-end as in **Fig. S3A, right, a blue graph**. Note that, for the p150 CC1-end-His and the p150 CC2-start-His, the origins were set at the barbed-end of the Arp1 rod, which was different from the previous measurements (**Fig. 3D** and **Fig. 4B**, respectively). The radial and angular lines represent the SD of the measurement and their cross points indicate the mean value (listed in **Table S2**). (B) The range of distributions of gold nanoparticles for four representative mutants. SDs of the nanogold distributions for four mutants, calculated by root mean squared distance, are shown as radii of circles around the centroids. SDs are 12.9 nm (N= 74), 4.3 nm (N= 95), 10.9 nm (N= 98) and 7.4 nm (N= 64) for p150-N-His, p150 CC2-start-His, p150-C-His and p50-N-His, respectively. Original plot data were shown in **Figs. 2B**, **4B**, **2D** and **5B** for p150-N-His, p150 CC2-start-His, p150-C-His and p50-N-His, respectively.

Saito et al. –Fig. S7

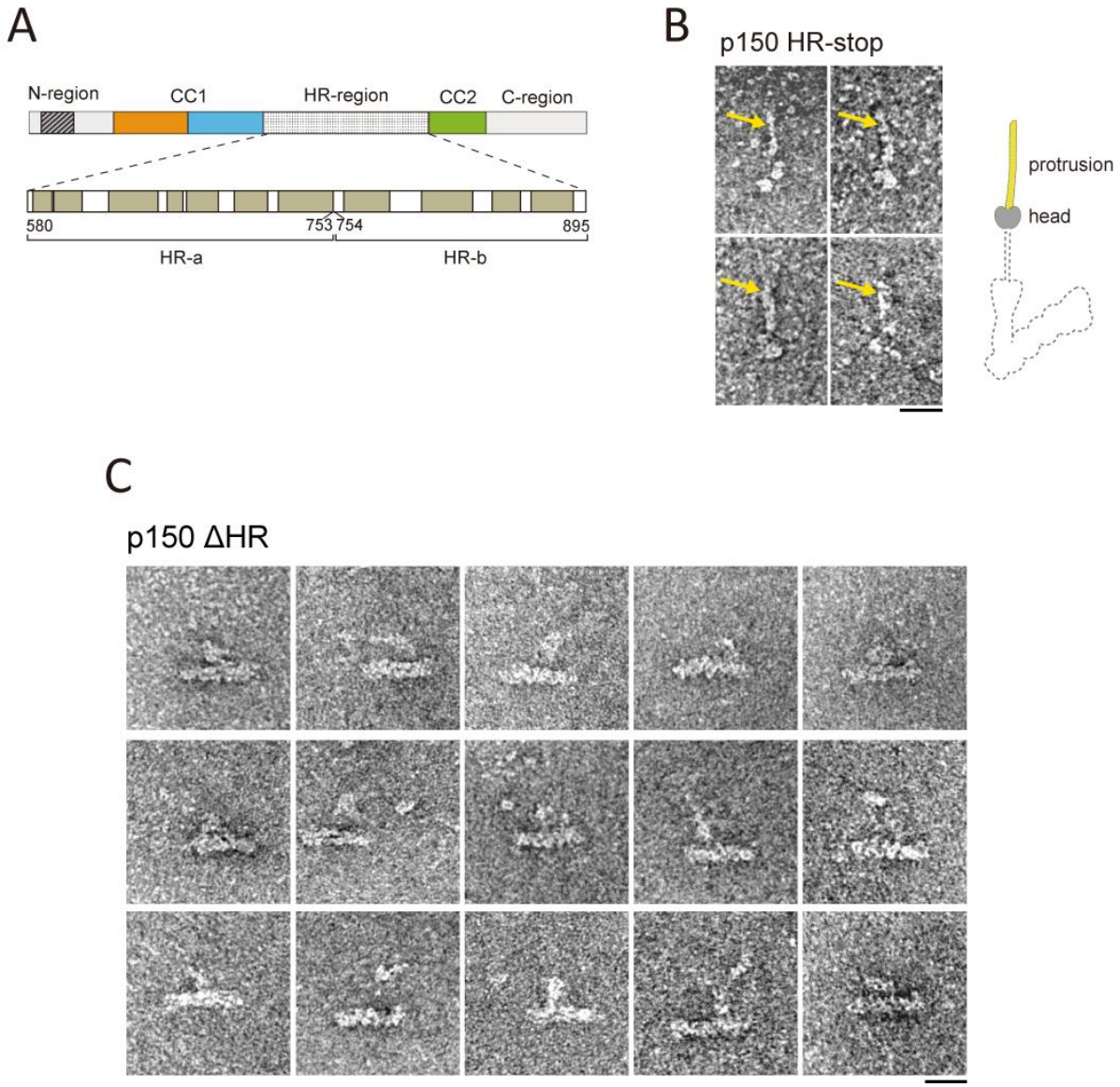

Figure S7. Structural contribution of the HR region to the head. (A) Secondary structure prediction of the HR region. The ochre gray colored regions of the sequence are predicted to form helices. (B) EM images of p150 HR-stop, which lacks the CC2 and the C-region. The protrusions formed by the CC1 (yellow arrows) are observed. The neck structures are conspicuous in the CC2-stop (**Fig. 5C, light blue arrows**) but not observed in this mutant. (C) A gallery of EM images of p150 ΔHR. Bars represent 20 nm.

Saito et al. –Table S1

No.	%Cov (95)	Accession #	Name	Peptides (95%)
1	45.6	Q14203	Dynactin subunit 1 (DCTN1)	56
5	70.1	Q13561	Dynactin subunit 2 (DCTN2)	28
7	60.1	P61163	Alpha-centractin (ACTR1A)	24
8	54.1	Q9UJW0	Dynactin subunit 4 (DCTN4)	14
9	47.9	O75935	Dynactin subunit 3 (DCTN3)	10
10	22.1	P63261	Actin, cytoplasmic 2 (ACTG1)	7
12	19.2	Q9NZ32	Actin-related protein 10 (ACTR10)	6
13	53.7	P42025	Beta-centractin (ACTR1B)	20
14	41.6	P52907	F-actin-capping protein subunit alpha-1 (CAPZA1)	5
15	23.9	P47756-2	Isoform 2 of F-actin-capping protein subunit beta (CAPZB)	5
17	8.5	P11142	Heat shock cognate 71 kDa protein (HSPA8)	4
18	22.1	O00399	Dynactin subunit 6 (DCTN6)	3
19	21	P47755	F-actin-capping protein subunit alpha-2 (CAPZA2)	3
20	7.8	Q9H3G5	Probable serine carboxypeptidase CPVL (CPVL)	3
21	3.1	Q8WWM7	Ataxin-2-like protein (ATXN2L)	2
22	19.8	Q9BTE1	Dynactin subunit 5 (DCTN5)	3
23	8.5	O95721	Synaptosomal-associated protein 29 (SNAP29)	2
24	22.1	P60709	Actin, cytoplasmic 1 (ACTB)	7
25	2.5	P02768	Serum albumin (ALB)	1
26	1.7	Q86YZ3	Hornerin (HRNR)	1
29	6.1	P08107	Heat shock 70 kDa protein 1A/1B (HSPA1A)	3
30	10.5	P07477	Trypsin-1 (PRSS1)	12
31	1.9	Q8N9M1	REVERSED Uncharacterized protein C19orf47 (C19orf47)	1
32	0.5	Q5D862	Filaggrin-2 (FLG2)	1
33	12.5	P62987	Ubiquitin-60S ribosomal protein L40 (UBA52)	1

Table S1. List of the proteins in the purified fraction of recombinant dynactin identified by LC-MS/MS spectrometry. Summary of proteins identified in the purified dynactin (SBP-p62). Keratin was removed from the list for simplification. %Cov (95) represents the percentage of matching amino acids from identified peptides having confidence greater than or equal to 95%, divided by the total number of amino acids in the sequence. Peptides (95%) represents the number of distinct peptide having 95% confidence.

Saito et al. –Table S2

Constructs	r (nm)	θ(°)	*N*
p150 CC1-end-His	39.2 ± 9.9	58 ± 34	94
p150 CC2-start-His	30.6 ± 8.1	57 ± 33	108
p150 CC2-end-His	22.5 ± 5.7	52 ± 20	95
p150-C-His	15.2 ± 7.3	55 ± 22	98
p50-N-His	9.3 ± 4.5	36 ± 30	64
p24-N-His	7.8 ± 4.1	29 ± 31	32

Table S2. Positions of the labeled gold nanoparticles in polar coordinates. Related to **Fig.S6A**. Distance (r) and angle (θ) are measured for each binding gold nanoparticle as described in **Fig. 2D**, and are shown as mean ± SD.

Saito et al. –Table S3

Name	Forward primer	Reverse primer	Methods
p150 CC1-start-His	5'-CATCACCATCACGGAGGTGGTTCC GAGGAGGAGGGACTAAGGGC-3'	5'-GTGATGGTGATGTGATCCACCTCC CTTGGATGGGGAAGGAAGCG-3'	Insertion
p150 C1-hinge-His	5'-CATCACCATCACGGAGGTGGTTCC CAGGAGCATGTGAAGCTCCA-3'	5'-GTGATGGTGATGTGATCCACCTCC CTTCTCTGAGGAAGAAAGAT-3'	Insertion
p150 CC1-end-His	5'-CATCACCATCACGGTGGAGGTTCA CAGCCACCTCCAGAGACCTT-3'	5'-GTGATGGTGATGTGATCCACCTCC CTGTTGCCTCTCCACAGATG-3'	Insertion
p150ΔCC1	5'-CCACCTCCAGAGACCTTTGAC-3'	5'-TGGGGAAGGAAGCGGGGGGAC-3'	Deletion
p150 CC2-start-His	5'-CATCACCATCACGGAGGTGGTTCC CGGCCCCCCAGCAAGCCTCC-3'	5'-GTGATGGTGATGTGATCCACCTCC CTCTGCATCATACTCCCCCT-3'	Insertion
p150 CC2-end-His	5'-CATCACCATCACGGAGGTGGTTCC GGACTCCGGGGCCCTCCTCC-3'	5'-GTGATGGTGATGTGATCCACCTCC CTCAATCGTGCGTTTGGACT-3'	Insertion
p150 ΔCC2	5'-GGACTCCGGGGCCCTCCTCCT-3'	5'-CTCTGCATCATACTCCCCCTC-3'	Deletion
p150 ΔHR	5'-CGGCCCCCCAGCAAGCCTCCA-3'	5'-TGGCCGAAGGAAGCTGTCAGG-3'	Deletion
p150 ΔHR-a	5'-GGGCAGGAGGCTACAGATATT-3'	5'-TGGCCGAAGGAAGCTGTCAGG-3'	Deletion
p150 ΔHR-b	5'-CGGCCCCCCAGCAAGCCTCCA-3'	5'-ACCCTGCAAGAAGGCACGCAG-3'	Deletion
p135	5'-AAGACCACAACTCGGCGACCCAA GCCCACGCGCCCAGCCAGTAC-3'	5'-TCGGGCTGTCGGTGCCTGTCTCAT GGTACCTCCAGAGCCTCCAT-3'	Insertion
p150 CC2-stop	5'-CTGGGATCCCAGCTGCACTGG-3'	5'-GGACGCGTTATCCCTCAATCGTGC GTTTGGA-3'	Truncation
p150 HR-stop	5'-CTGGGATCCCAGCTGCACTGG-3'	5'-GGACGCGTTATGCATCATACTCCC CCTCCTG-3'	Truncation

Table S3. List of primers used for construction of p150 mutants.